Research Square

Preprints are preliminary reports that have not undergone peer review.
They should not be considered conclusive, used to inform clinical practice,
or referenced by the media as validated information.

Spin-Coating-Speed-Dependent Structural and Optical Properties of Open-Air-Processed MAPbI 3 Thin Films with Bandgap-Constrained SCAPS-1D Sensitivity Analysis

Aaron Aransiola

aaransiola@oauife.edu.ng

Obafemi Awolowo University, Nigeria

Peverga Jubu

Joseph Sarwuan Tarka University Makurdi, Nigeria

Chijioke Amakom

Africa Centre of Excellence in Future Energies and Electrochemical Systems, FUTO

Kufre Udofia

Africa Centre of Excellence in Future Energies and Electrochemical Systems, FUTO

Izuchukwu Nwokolo

Africa Centre of Excellence in Future Energies and Electrochemical Systems, FUTO

Adamu Goje

Africa Centre of Excellence in Future Energies and Electrochemical Systems, FUTO

John Anyanwu

Africa Centre of Excellence in Future Energies and Electrochemical Systems, FUTO

Ike hukwu Ayogu

Africa Centre of Excellence in Future Energies and Electrochemical Systems, FUTO

Kanayo Oguzie

Africa Centre of Excellence in Future Energies and Electrochemical Systems, FUTO

Muhammad Kuranga

Africa Centre of Excellence in Future Energies and Electrochemical Systems, FUTO

Olusoji Ilori

Obafemi Awolowo University, Nigeria

Samuel Olayiwola

Obafemi Awolowo University, Nigeria

Oluwakayode Fadahunsi

Obafemi Awolowo University, Nigeria

Chinyere Madu

Africa Centre of Excellence in Future Energies and Electrochemical Systems, FUTO

Emeka Oguzie
Africa Centre of Excellence in Future Energies and Electrochemical Systems, FUTO

Research Article

Keywords: $MAPbI_3$ thin films, spin-coating speed, ambient-air processing, optical bandgap, SCAPS-1D, perovskite solar cells

Posted Date: November 13th, 2026

DOI: https://doi.org/10.21203/rs.3.rs-11458197/v1

License: This work is licensed under a Creative Commons Attribution 4.0 International License.
Read Full License

Additional Declarations: No competing interests reported.

Spin-Coating-Speed-Dependent Structural and Optical Properties of Open-Air-Processed $MAPbI_3$ Thin Films with Bandgap-Constrained SCAPS-1D Sensitivity Analysis

Aaron O. Aransiola[a, b], Peverga R. Jubu[b,c], Chijioke Amakom[b,d], Kufre I. Udofia[b] Izuchukwu K. Nwokolo[b], Adamu Ahmed Goje[b,e] ,John O. Anyanwu[b], Ikechukwu I. Ayogu[b], Kanayo Lucy Oguzie[b], Muhammad B. Kuranga[b,f],Olusoji O. Ilori[a], S. P. Olayiwola[a], O. O. Fadahunsi[a], Chinyere A. Madu[b], Emeka E. Oguzie[b]

[a]Electronic and Electrical Engineering Department, Obafemi Awolowo University, Ile-Ife, Osun State, Nigeria

[b]Africa Centre of Excellence in Future Energies and Electrochemical Systems (ACE-FUELS), Federal University of Technology Owerri (FUTO), P.M.B. 1526 Owerri, Imo State, Nigeria.

[c]Department of Industrial Physics, Joseph Sarwuan Tarka University (University of Agriculture Makurdi), P.M.B. 2373 Makurdi, Benue State, Nigeria

[d]Department of Physics, Federal University of Technology Owerri (FUTO), P.M.B. 1526 Owerri, Imo State, Nigeria

[e]Department of Applied Physics, Federal Polytechnic Damaturu, Damaturu, Yobe State, Nigeria

[f]National Agency for Science and Engineering Infrastructure (NASENI) Abuja, Nigeria

Corresponding authors: emeka.oguzie@futo.edu.ng (E.E. Oguzie), aaransiola@oauife.edu.ng (A.O. Aransiola), peverga.jubu@uam.edu.ng (P.R. Jubu)

Abstract

Spin coating offers an accessible route for depositing metal-halide perovskite absorbers, but interactions among rotational speed, solvent removal and crystallization complicate ambient process optimization. This study examined the effects of spin-coating speed (2000–5000 rpm) on the structural and optical properties of open-air-processed methylammonium lead iodide ($MAPbI_3$) films and used measured optical bandgaps to constrain SCAPS-1D simulations. Films were deposited from a 1.25 M precursor using ethyl acetate antisolvent treatment and annealed at 110 °C for 10 min under controlled conditions of 24.4 °C and 41.5% relative humidity. X-ray diffraction confirmed tetragonal $MAPbI_3$ with preferential (110) orientation and no detectable PbI_2 reflection. The structural response was non-monotonic. At 3000 rpm, the film exhibited the narrowest (110) peak (FWHM: 0.352°), largest Scherrer coherent-domain size (22.73 nm), lowest estimated microstrain (1.257×10^{-2}) and lowest crystallographic dislocation-density parameter (1.936×10^{-3} nm^{-2}). Thus, 3000 rpm produced the most favourable XRD-derived crystalline characteristics within the investigated range, although these metrics do not establish reduced

electronic trap density, suppressed recombination or superior photovoltaic performance. Optical bandgaps ranged from 1.59-1.60 eV. In an otherwise fixed FTO/TiO_2/$MAPbI_3$/Spiro-OMeTAD/carbon model, the corresponding simulated efficiencies were 16.67% and 16.47%, respectively. Coordinated parameter optimization yielded a projected efficiency of 25.38%, with V_{oc} of 1.25 V, J_{sc} of 24.24 mA cm^{-2} and fill factor of 83.61%. These results establish a process-specific structure–optical-property relationship, while the simulated outputs remain model-dependent projections requiring experimental device validation. The approach also illustrates how experimental measurements can inform device-level sensitivity analysis without overstating causal relationships.

Keywords:

$MAPbI_3$ thin films; spin-coating speed; ambient-air processing; optical bandgap; SCAPS-1D; perovskite solar cells

Introduction

Metal-halide perovskite solar cells have developed rapidly from the first photovoltaic use of organolead halide perovskites to a versatile thin-film technology with exceptional optoelectronic performance [1–3]. Their appeal arises from strong visible-light absorption, a direct and compositionally tunable bandgap, long carrier-diffusion lengths, low exciton-binding energy and compatibility with low-temperature solution processing [4–6]. These attributes offer a pathway to lightweight and potentially low-cost photovoltaics. Nevertheless, the translation of high material quality into reproducible device performance remains limited by the sensitivity of the perovskite layer to precursor chemistry, solvent coordination, crystallization kinetics, environmental conditions and interfaces [3,6,7].

Methylammonium lead iodide ($CH_3NH_3PbI_3$, $MAPbI_3$) remains an important model absorber for studying process–structure–property relationships in lead-halide perovskites. It normally exhibits a direct optical bandgap near 1.55–1.60 eV, a sharp absorption edge and strong absorption throughout much of the visible spectrum [5,8]. Although more compositionally complex perovskites have achieved greater operational stability, $MAPbI_3$ offers comparatively simple precursor stoichiometry and well-established structural and optical signatures. It is therefore

particularly useful for isolating how a deposition variable modifies crystallinity, defect formation, optical response and the photovoltaic quantities predicted from those properties.

Spin coating is widely employed for laboratory-scale perovskite deposition because it enables rapid control of solution spreading, wet-film thinning and solvent evaporation. During rotation, centrifugal flow, viscous resistance and solvent loss collectively determine the final thickness and uniformity of the coating; film thickness commonly decreases with increasing angular velocity according to a process-dependent power-law relationship [9]. In perovskite precursor films, however, rotational speed does more than change thickness. It also changes the residence time of coordinating solvents, precursor supersaturation, nucleation density and the interval available for crystal growth. A speed that is too low may leave a thick wet layer that dries non-uniformly, whereas excessive speed can remove solution and solvent so rapidly that crystal coalescence is restricted. An intermediate speed can consequently provide the best compromise between coverage, nucleation and grain development.

Solvent and antisolvent engineering further govern this kinetic competition. Coordinating solvents such as dimethyl sulfoxide can form intermediate adducts with lead-halide precursors, slowing uncontrolled crystallization, while timely antisolvent application rapidly extracts the host solvent and drives the wet film towards supersaturation [10,11]. The identity, volume, timing and delivery position of the antisolvent must therefore be controlled alongside spin speed. Recent ambient-processing studies have confirmed that antisolvent selection can substantially change perovskite phase formation, surface coverage and optical response [12], and that single-step $MAPbI_3$ deposition in air requires coordinated optimization of precursor temperature, solvent composition, spin parameters and annealing conditions [13].

Ambient fabrication adds another important source of variability. Water vapour can alter precursor coordination, intermediate-phase formation, nucleation and annealing behaviour, with the outcome depending on humidity level and the specific processing route [7,14]. Reproducible open-air studies should therefore report temperature and relative humidity rather than treating the surrounding atmosphere as an unspecified background condition. Establishing a process window under measured ambient conditions is particularly important for laboratories and future manufacturing environments where continuous inert-atmosphere control may be technically or economically restrictive.

The structural consequences of deposition can be evaluated from X-ray diffraction through phase identity, preferred orientation, peak width and derived microstructural parameters. For tetragonal $MAPbI_3$, the intense reflections near 14° and 28° are commonly associated with the (110) and (220) planes, whereas a reflection near 12.6° can indicate residual PbI_2. Peak broadening may be used to estimate coherent crystallite size, although strain and instrumental broadening should be considered when interpreting Scherrer-derived values. Although XRD-derived peak width, coherent crystallite size and microstrain provide useful measures of long-range crystalline order, they do not directly quantify electronically active point defects or deep-level trap states. Consequently, favourable XRD characteristics cannot, by themselves, establish reduced non-radiative recombination or superior photovoltaic performance. Such relationships require corroboration through carrier-dynamics, defect-density, electrical or complete-device measurements.

Optical spectroscopy provides complementary information because deposition-induced differences in thickness, coverage, scattering and structural disorder modify absorbance and the apparent absorption edge. Accurate bandgap comparison consequently requires consistent baseline correction and use of the measured thickness when calculating the absorption coefficient [5,8].

Experimental characterization alone does not directly reveal how a small change in bandgap or defect-related material quality propagates through a complete photovoltaic stack. SCAPS-1D addresses this limitation by solving Poisson's equation together with carrier-continuity and drift–diffusion equations for multilayer thin-film devices [15,16]. It permits independent examination of absorber thickness, band alignment, doping, carrier mobility, bulk and interface defect densities, contact properties and parasitic resistances. Studies have combined experimental $MAPbI_3$ data with SCAPS-1D modelling to connect measured absorber properties with prospective device performance [17]. However, simulated efficiencies should be interpreted as model-dependent projections rather than experimental device records, particularly when parameters are optimized independently of demonstrated processing constraints.

Many reports optimize either $MAPbI_3$ film preparation or numerical device parameters, but fewer establish a direct experimental-to-simulation workflow in which a deliberately varied deposition parameter is linked to measured structural and optical responses and then introduced into device modelling. Moreover, apparently simple trends with spin speed may conceal a non-monotonic crystallization response. This makes it necessary to distinguish the experimentally observed effect

of deposition speed from subsequent numerical sensitivity analyses in which other layer and device parameters are varied.

Accordingly, this study investigates $MAPbI_3$ films deposited in open air at 2000, 3000, 4000 and 5000 rpm while holding precursor concentration and volume, acceleration, coating duration, ethyl acetate antisolvent treatment, annealing conditions and the measured cleanroom environment constant. The films are compared using X-ray diffraction and UV–visible spectroscopy to establish their phase, crystallite-related parameters and optical bandgaps. The experimentally obtained bandgaps are subsequently incorporated into a planar $FTO/TiO_2/MAPbI_3$/Spiro-OMeTAD/carbon SCAPS-1D model. Parametric analyses of layer thickness, carrier density, bulk and interface defects, series and shunt resistance, and temperature are then used to identify the dominant performance limitations and a physically interpretable route towards an optimized device.

2. 0 Materials synthesis and Methods

2.1 ITO Substrate Preparation and Cleaning

Patterned indium tin oxide (ITO)-coated glass substrates for photovoltaic and organic light-emitting diode applications were obtained from Ossila Ltd. (product code S2006C1; batch number: 250428-01F). Each substrate measured $25\,mm \times 25\,mm$, nominal sheet resistance of $20\,\Omega/sq$ and had a glass thickness of $1.1\,mm$. Prior to the deposition of the perovskite layer, the substrates were sequentially cleaned using a Digital Pro+ digital ultrasonic cleaner equipped with independently adjustable bath-temperature and sonication-time controls. The substrates were initially ultrasonicated for $15\,min$ in a 1:4 (v/v) Hellmanex™ III/deionized-water solution prepared using Hellmanex™ III critical-cleaning concentrate (Ossila Ltd.; product code C141-25mL). The deionized water used throughout the cleaning process had an electrical conductivity of $0.999\,\mu S$ cm^{-1}, an electrical resistivity of $0.52\,M\Omega$ cm, and a total dissolved solids concentration of $0.499\,ppm$, as indicated by the integrated conductivity/resistivity meter of the BIOBASE water-purification system. Following this treatment, the substrates were thoroughly rinsed with fresh deionized water to remove residual alkaline cleaning agents. The substrates were subsequently ultrasonicated sequentially in deionized water, acetone (BDH; GPR grade; minimum assay 99.5 %) and isopropyl alcohol, also referred to as propan-2-ol (BDH; GPR grade; minimum

assay 99.5 %), for 10 min in each cleaning medium. All ultrasonication steps were performed at 50 °C, with thorough rinsing using fresh portions of the corresponding cleaning liquid between successive stages. This procedure facilitated the removal of dust particles, grease, organic residues and other surface contaminants from the ITO surface. Following solvent cleaning, the substrates were dried under a stream of high-purity nitrogen gas (N_2, 99.99 % purity) to remove residual solvent and loosely bound surface particles. They were subsequently treated in an Ossila UV–ozone cleaner for 10 min as the final surface-cleaning step. The UV–ozone treatment removed residual organic contaminants and increased the surface energy and wettability of the ITO, thereby promoting improved interfacial contact and more uniform deposition of the subsequent functional layers. The cleaned substrates were used immediately for thin-film deposition to minimize surface recontamination.

2.2 Preparation of $MAPbI_3$ Perovskite Precursor Solution

A 1.25 M $MAPbI_3$ precursor solution was prepared by dissolving 0.864 g (1.874 $mmol$) of lead(II) iodide (PbI_2; Sigma-Aldrich; 99 % purity, corresponding to a maximum nominal impurity content of 1 %; product no. 211168) and 0.298 g (1.875 $mmol$) of of methylammonium iodide (MAI: recrystallised, >99.5 % purity; Ossila Ltd.; product code M271-5g) in 1.2 mL of N,N-dimethylformamide (DMF; Molychem India LLP; LR grade; minimum assay 99 %, maximum nominal impurity content 1 %; product code 14185) and 0.3 mL of dimethyl sulfoxide (DMSO; Molychem India LLP; LR grade; minimum assay 99 %, maximum nominal impurity content 1 %; product code 14187)., producing a total solvent volume of 1.5 mL and an approximately equimolar PbI_2:MAI ratio of 1:1. The resulting DMF:DMSO volume ratio was 4:1. The solution was magnetically stirred at 60 °C for 10 min to facilitate complete dissolution and homogenization. Before spin-coating deposition, the precursor solution was passed through a 0.45 μm polyvinylidene fluoride (PVDF) syringe filter to remove undissolved particles and aggregates that could cause pinholes, nonuniform nucleation and local variations in film thickness. The precursor preparation was conducted in a cleanroom under an intelligent air-purification fume hood. The recorded environmental and processing conditions were a relative humidity of 41.5 %, an ambient temperature of 24.4 °C, a fume-hood face velocity of 0.29 $m\,s^{-1}$ and a total volatile organic

compound concentration of 1 ppm. All recorded chemicals were used as received without further purification.

2.3 Spin coating and thermal annealing of $MAPbI_3$ films

The $MAPbI_3$ precursor solution was deposited onto the cleaned ITO substrates using a VTC-100PA vacuum spin coater under the same cleanroom conditions employed for precursor preparation: 41.5 % relative humidity, 24.4 $°C$ ambient temperature, 0.29 $m\ s^{-1}$ fume-hood face velocity and 1 ppm TVOC. For each sample, 100 µL of the precursor solution was applied to the centre of the stationary substrate using the static-dispensing method before applying the spin-coating conditions presented in Table 1. This method was selected to promote complete initial surface coverage, minimize precursor loss and improve the reproducibility of radial spreading and film formation. Following precursor application, the spin-coating programme was initiated immediately to limit uncontrolled solvent evaporation and premature crystallization. Ethyl acetate (EA, 300 µL) was employed as the antisolvent to induce rapid solvent extraction, precursor supersaturation and perovskite nucleation. The antisolvent was dispensed at the centre of the rotating substrate at $t = 15\ s$ after initiation of the 30 s spin-coating cycle, corresponding to the beginning of the final 15 s. It was delivered as a single continuous dispense rather than as multiple discrete drops, while the micropipette tip was maintained approximately 1 cm above the substrate. Continuous central dispensing promoted rapid and relatively uniform antisolvent distribution across the rotating wet film, minimized localized solvent-extraction gradients and avoided repeated impact disturbances that could cause splashing, film displacement, nonuniform nucleation or thickness variations. Spin speed was the deliberately varied deposition parameter; precursor formulation and volume, acceleration/deceleration, total duration, antisolvent identity, volume, timing and delivery geometry, annealing conditions and environment were held constant.

Table 1. Spin-coating conditions used for $MAPbI_3$ film deposition.

Sample ID	Spin speed (rpm)	Acceleration/eleration (rpm s^{-1})	Duration (s)	Antisolvent treatment (µL)
S1	5000	2000	30	300
S2	4000	2000	30	300

Sample ID	Spin speed (rpm)	Acceleration/eleration (rpm s^{-1})	Duration (s)	Antisolvent treatment (μL)
S3	3000	2000	30	300
S4	2000	2000	30	300

Immediately after spin coating, the wet films were transferred onto a preheated hotplate and annealed at $110\ °C$ for $10\ min$. Thermal annealing promoted the evaporation of residual DMF, DMSO and antisolvent, the conversion of the intermediate precursor phase into crystalline $MAPbI_3$, and the development of the characteristic dark perovskite film. Following annealing, the samples were allowed to cool naturally to room temperature before storage or further characterization.

2.4 Structural and Optical Characterization of $MAPbI_3$ Thin Films

The structural and optical properties of the $MAPbI_3$ absorber layers were investigated using X-ray diffraction (XRD) and UV–Vis spectroscopy, respectively. The crystalline structure and phase formation were examined using an Aeris benchtop X-ray diffractometer (Malvern Panalytical, the Netherlands; Type No. 9430 070 99991). The XRD patterns are displayed over 10–60° for clarity; although measurements were acquired over 5–90°; using Cu Kα radiation ($K\alpha_1$, $\lambda = 1.540598$ Å), with a step size of 0.0108664° in continuous-scan mode. The instrument data file recorded a time-per-step value of 48.195. The resulting diffraction patterns were analysed to identify the crystalline $MAPbI_3$ phase, preferred crystallographic orientation, and the possible presence of residual precursor or secondary phases. Particular attention was given to the positions and relative intensities of the characteristic $MAPbI_3$ diffraction reflections. The full width at half maximum (FWHM) of selected diffraction peaks was determined from the XRD patterns and subsequently used for crystallite-size and related structural analyses.

The wavelength-dependent optical response of the $MAPbI_3$ thin films was characterised using a PerkinElmer LAMBDA 365+ UV–Vis spectrophotometer controlled with UV WinLab software. Absorbance, transmittance, and reflectance spectra were recorded over the wavelength range of $200 - 1100\ nm$, with the instrument scanning from $1100\ to\ 200\ nm$. A spectral bandwidth of $1.00\ nm$, scan speed of $480\ nm\ min^{-1}$, and data interval of 1 nm were employed. Each $MAPbI_3$

thin film was measured using a single scan cycle with a cycle time of 1 s. Both the UV and visible lamps were activated during measurement, with automatic lamp changeover at $400\,nm$. The recorded spectra were subsequently analysed to evaluate the wavelength-dependent optical behaviour of the films, determine the absorption edge, and estimate the optical bandgap of $MAPbI_3$.

2.5 Numerical simulation of perovskite solar cell

Numerical simulation of the perovskite solar cell was performed to investigate how the experimentally determined optical bandgap of the $MAPbI_3$ absorber influences the photovoltaic performance of the proposed device. The simulated cell employed the conventional n–i–p configuration:

FTO/TiO_2/$MAPbI_3$/Spiro-OMeTAD/Carbon

Numerical device modelling provides insight into the physical processes governing charge generation, transport, recombination and collection within the solar cell. It also enables systematic evaluation of material and device parameters that may be difficult to vary independently during experimental fabrication.

The simulations were carried out using the one-dimensional Solar Cell Capacitance Simulator, SCAPS-1D. The software was developed at Ghent University, Belgium, by Burgelman and co-workers for the numerical analysis of thin-film semiconductor devices. SCAPS-1D calculates the steady-state electrical and optoelectronic behaviour of a multilayer device by simultaneously solving Poisson's equation, the electron and hole continuity equations, and the drift–diffusion current-density equations under specified boundary and operating conditions.

The simulation procedure accounts for the thickness, bandgap, electron affinity, dielectric permittivity, effective density of states, charge-carrier mobility, doping concentration and defect density of each semiconductor layer. It can also incorporate interface defect states, bulk recombination, contact work functions, series resistance and shunt resistance. From these inputs, SCAPS-1D predicts the current density–voltage characteristics, external quantum efficiency, energy-band profile, carrier concentrations, generation and recombination rates, capacitance–voltage response and capacitance–frequency behaviour of the device [19][20][21].

The electrostatic potential within the device is governed by Poisson's equation (Eq. 1).

$$\frac{d^2\psi(x)}{dx^2} = -\frac{q}{\varepsilon}[p - n + N_D^+ - N_A^- + p_t - n_t]\,, \qquad 1$$

where, ψ represent the electrostatic potential, ε denote dielectric constant of the semiconductor equal to $\varepsilon = \varepsilon_r\varepsilon_0$, where ε_r is the relative permittivity and ε_0 is vacuum permittivity, q symbolize electron charge, N_A^- and N_D^+ are acceptor and donor carrier density, respectively, E is the electric field, p and n are the hole and electron concentration, n_t and p_t are the trapped electron and hole concentration, respectively.

The steady-state electron and hole continuity equations are expressed as in Eqs. 2 and 3:

$$\frac{1}{d}\frac{dJ_n}{dx} = G_n - R_n, \qquad 2$$

$$\frac{1}{d}\frac{dJ_p}{dx} = G_p - R_p, \qquad 3$$

where J_n and J_p are the electron and hole current densities, G_n and G_p are the electron and hole generation rates, and R_n and R_p represent the corresponding recombination rates.

The electron and hole current densities are described by the drift–diffusion relation (Eqs.4 and 5).

$$J_n = qn\mu_n E + qD_n\frac{dn}{dx}, \qquad 4$$

$$J_p = qp\mu_p E - qD_p\frac{dp}{dx}, \qquad 5$$

$$D_{n,p} = \left(\frac{k_B T}{q}\mu_{n,p}\right), \qquad 6$$

where E is the electric field, μ_n and μ_p are the electron and hole mobilities, and D_n and D_p are the electron and hole diffusion coefficients. The diffusion coefficients are related to the carrier mobilities through the Einstein relation (Eq. 6), where k_B is the Boltzmann constant and T is the absolute temperature.

2.5.1 Device structure and operating mechanism

The simulated perovskite solar cell shown in Fig.1 employs the planar n–i–p configuration FTO/TiO_2/$MAPbI_3$/Spiro-OMeTAD/Carbon. FTO acts as the transparent front electrode, while TiO_2 selectively extracts electrons and blocks holes. $MAPbI_3$ serves as the light-absorbing layer in which electron–hole pairs are generated. Spiro-OMeTAD extracts holes and suppresses electron transfer towards the rear contact, whereas carbon collects the holes and functions as the back electrode. Under illumination, electrons move from $MAPbI_3$ through TiO_2 to FTO, while holes move from $MAPbI_3$ through Spiro-OMeTAD to carbon [22].

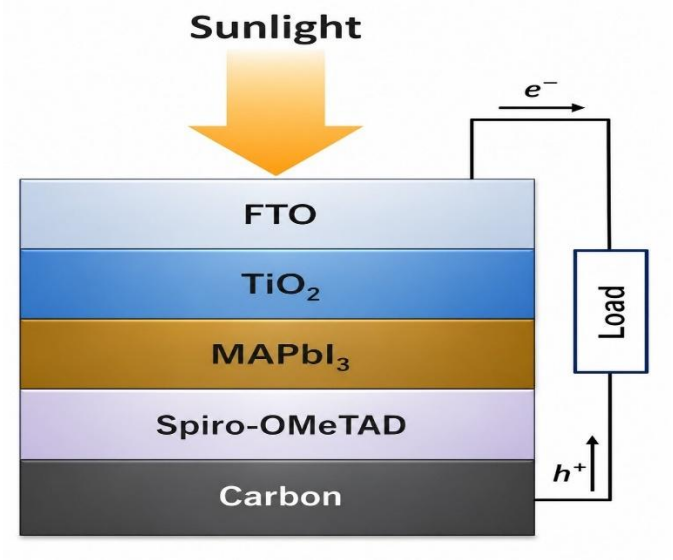


Fig. 1. Schematic diagram of the simulated PSC.

2.5.2 Basic input parameters and simulation conditions

The SCAPS-1D model was constructed using the thickness, bandgap, electron affinity, relative dielectric permittivity, effective density of states, carrier mobility, doping concentration and bulk defect density of the constituent device layers, as summarized in Table 2. The experimentally measured $MAPbI_3$ bandgap values of $1.59 - 1.60\ eV$ were incorporated into the model to evaluate the influence of the deposition conditions on photovoltaic performance. Defect states were introduced at the TiO_2/$MAPbI_3$ and $MAPbI_3$/Spiro-OMeTAD interfaces to account for non-ideal interfacial recombination; the corresponding interface parameters are presented in Table 3. The work functions of the carbon and FTO contacts were set to $5.0\ eV$ and $4.4\ eV$, respectively [19][21]. Simulations were performed under AM1.5G illumination at an incident power density of $100\ mW\ cm^{-2}$, an operating temperature of $300\ K$, and a voltage range of $0 - 1.50\ V$ [19][21].

Table 2. SCAPS-1D parameters for simulating the structure of the PSC [21][23][24]

Parameters	Layer			
	FTO	TiO_2 [23]	Spiro-OMeTAD [21]	$MAPbI_3$ [24]
Thickness (μm)	0.1	0.06	0.05	0.5
E_g (eV)	3.5	3.2	2.9	1.59, 1.60
ε_r	9.0	10.0	2.2	6.5
χ (eV)	4.3	4.2	3.0	3.9
N_C (cm^{-3})	2.2×10^{18}	2.2×10^{18}	2.2×10^{18}	2.2×10^{18}
N_V (cm^{-3})	1.8×10^{19}	1.8×10^{19}	1.8×10^{19}	1.8×10^{19}
N_A (cm^{-3})	0	0	1×10^{18}	1×10^{16}
N_D (cm^{-3})	1×10^{18}	1×10^{18}	0	0
μ_n (cm^2V^{-1} s^{-1})	20	20	1×10^{-4}	2
μ_p (cm^2V^{-1} s^{-1})	10	10	2×10^{-4}	2
N_t (cm^{-3})	1×10^{15}	1×10^{15}	1×10^{15}	1×10^{14}
Defect type	Neutral	Single donor	Single acceptor	Single acceptor

Table 3. Interface layer parameters [21],[24]

Parameters	TiO_2/$MAPbI_3$ interface	$MAPbI_3$/Spiro-OMeTAD
Defect type	Neutral	Neutral
Cross section for electrons (cm^2)	1×10^{-19}	1×10^{-19}
Cross section for holes (cm^2)	1×10^{-19}	1×10^{-19}
Energetic distribution	Single	Single
Energy level with respect to E_V (eV)	0.65	0.65

Characteristic energy (eV)	0.10	0.10
Total density (cm^{-2})	1×10^{12}	1×10^{12}

The temperature dependence of the optimized device was evaluated from 290 to 340 K in 10 K increments. In this calculation, SCAPS-1D automatically varied the effective conduction- and valence-band densities of states, carrier thermal velocities, thermal voltage and diffusion coefficients. All user-defined material and device parameters, including bandgap, electron affinity, dielectric permittivity, carrier mobility, doping concentration, defect density, defect-energy level, capture cross-section, layer thickness, contact work function, optical-absorption input, series resistance and shunt resistance, were held constant. No explicit temperature-dependent bandgap, mobility or structural-phase-transition model was introduced. Therefore, the calculation represents a fixed-material temperature sensitivity analysis rather than a complete simulation of temperature-induced changes in $MAPbI_3$.

3.0 Results and discussion

3.1 Crystal structure

Fig. 2 presents the X-ray diffraction patterns of $MAPbI_3$ thin films as-deposited under varying spin coating speed. All the samples exhibit the characteristic diffraction reflections of crystalline $MAPbI_3$, confirming successful formation of the perovskite phase under the investigated open-air deposition conditions. The most intense peak occurs at $2\theta \approx 13.94–14.02°$ and is assigned to the (110) plane of tetragonal $MAPbI_3$. The persistence of this dominant reflection in all the films indicates preferential crystal growth along the (110) orientation, irrespective of the applied spin speed.

Additional $MAPbI_3$ reflections are observed at approximately 19.81°, 23.34°, 24.47°, 28.25°, 31.51°, 34.86°, 40.52°, 43.1° and 50.25°, corresponding approximately to the (112), (211), (202), (220), (310), (312), (224), (314) and (404) crystallographic planes, respectively. The strong (110) and (220) reflections confirm the formation of the tetragonal $MAPbI_3$ structure. The peak near 30.52–30.73°, particularly visible in the thinner films, is assigned mainly to the (222) reflection of the underlying ITO substrate rather than to $MAPbI_3$. Its visibility is likely enhanced at higher spin

speeds because faster rotation produces a thinner perovskite layer, allowing the substrate contribution to become more pronounced.

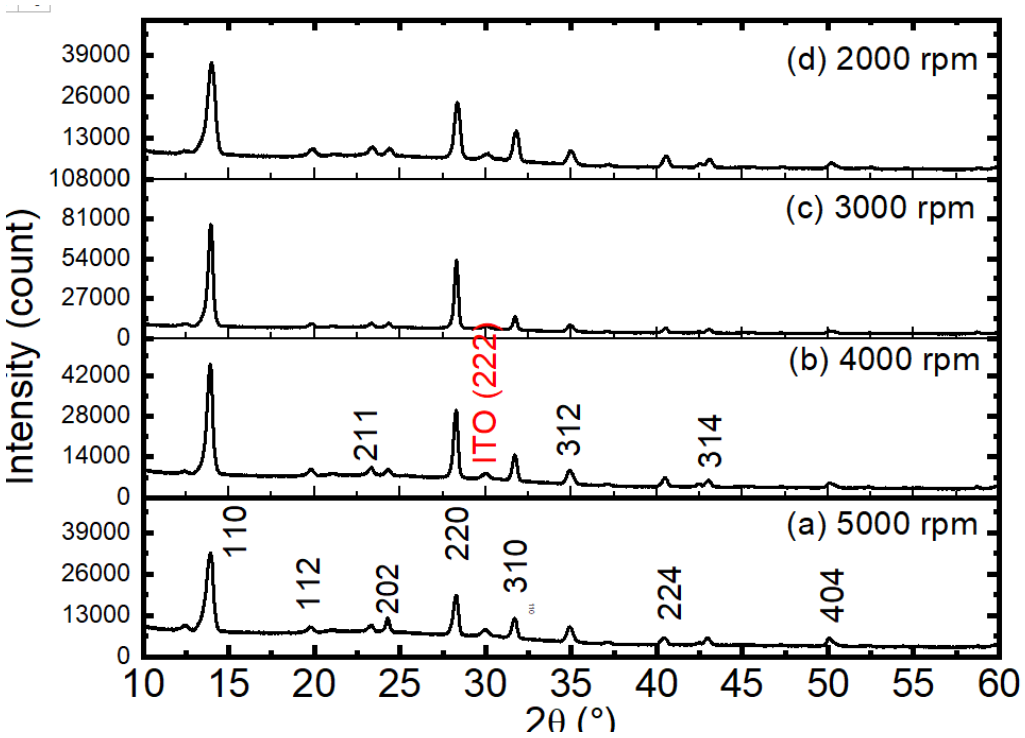


Fig. 2. XRD patterns of the samples deposited under varying speeds (a) 5000, (b) 4000, (c) 3000, (d) 2000 rpm.

No distinct diffraction peak is evident near 2θ≈ 12.63°, which is the principal (001) reflection of crystalline PbI_2. This suggests that the precursor materials were largely converted into $MAPbI_3$, with no appreciable residual PbI_2 detectable by XRD.

The structural parameters calculated from the dominant $MAPbI_3$ (110) reflection further demonstrate the influence of spin speed on crystal quality. The peak position changes only slightly from 13.94 to 14.02 °, indicating that deposition speed does not significantly alter the crystal phase. The small displacement of the peak may instead arise from minor changes in residual strain, lattice distortion or film–substrate interaction.

The $3000\ rpm$ film exhibits the smallest FWHM of 0.35211°, and consequently possesses the largest crystallite size of $22.732\ nm$. It also has the lowest microstrain of 1.257×10^{-2} and the

lowest crystallographic dislocation-density parameter of $1.936 \times 10^{-3}\ nm^{-2}$. These results indicate that deposition at 3000 rpm produced the narrowest measured peak and the most favourable derived crystallographic parameters.

At 4000 rpm, the FWHM increases to 0.42891°, giving a crystallite size of 18.66 nm, a microstrain of $1.532\times\ 10^{-2}$, and a crystallographic dislocation-density parameter of $2.872\times10^{-3}\ nm^{-2}$. Although the crystal quality remains reasonably high, the smaller crystallite size and increased strain relative to the 3000 rpm film suggest that faster solvent removal begins to restrict crystal growth.

The film deposited at 5000 rpm exhibited a broader (110) diffraction peak, with an FWHM of 0.58067°, corresponding to a Scherrer coherent-domain size of 13.78 nm. The broader peak is consistent with smaller coherent domains and/or greater lattice-strain broadening. Rapid film thinning and solvent removal at this rotational speed may have restricted crystal growth and coalescence; however, the individual contributions of coherent-domain size, microstrain and instrumental broadening cannot be conclusively separated using the present single-peak analysis.

Similarly, the film deposited at 2000 rpm exhibited the broadest (110) diffraction peak, with an FWHM of 0.60842° and a corresponding Scherrer coherent-domain size of 13.16 nm. The broader peak is consistent with smaller coherent domains and/or greater lattice-strain broadening. At this relatively low spin speed, the thicker wet precursor layer may have undergone less-uniform solvent removal and crystallization. Nevertheless, this proposed mechanism remains an interpretation because solvent-removal kinetics were not measured directly.

This non-monotonic behaviour indicates that an intermediate spin speed provides a better balance between film thinning, solvent evaporation, nucleation and grain growth. Among the investigated conditions, 3000 rpm produced the most favourable XRD-derived crystalline characteristics, including the largest Scherrer coherent-domain size and the lowest estimated microstrain and crystallographic dislocation-density parameter. These results indicate improved long-range lattice ordering within the sensitivity of XRD. However, they do not directly establish a reduction in electronically active point defects, deep-level traps or non-radiative recombination centres. Accordingly, the photovoltaic superiority of this deposition condition cannot be concluded from XRD measurements alone.

The crystallite size was determined using Debye–Scherrer equation (Eq. 7) [25]

$$D = \frac{K\lambda}{\beta \cos\theta} \qquad 7$$

where K = 0.9, λ = 0.15406 nm for Cu Kα radiation, β = FWHM in radians, and θ = 2θ/2, the crystallite sizes for the $MAPbI_3$ (110) peak are shown in Table 4. The Microstrain was evaluated by Eq. 8, while the crystallographic dislocation density was calculated using Eq. 9 [25] where D is the Scherrer coherent-domain size. It should be noted that this parameter was used only as a comparative indicator of XRD-derived crystalline order and should not be interpreted as the concentration of electronically active traps or as the absorber bulk-defect density employed in SCAPS-1D.

$$\varepsilon = \frac{\beta}{4 \tan\theta} \qquad 8$$

$$\delta = \frac{1}{D^2} \qquad 9$$

Table 4. XRD-derived structural parameters of $MAPbI_3$ films deposited at different spin-coating speeds.

Deposition speed (rpm)	Peak	2theta (°)	FWHM (°)	FWHM (rad)	Crystallite size (nm)	Microstrain, ε	Crystallographic dislocation-density parameter, $\delta\ (nm^{-2})$
5000	110	13.941	0.58067	0.01014	13.78	2.072×10^{-2}	5.264×10^{-3}
4000		13.930	0.42891	0.00749	18.66	1.532×10^{-2}	2.872×10^{-3}
3000		13.941	0.35211	0.00615	22.73	1.257×10^{-2}	1.936×10^{-3}
2000		14.017	0.60842	0.01062	13.16	2.160×10^{-2}	5.778×10^{-3}

3.2 Optical Properties

3.2.1 Effect of spin-coating speed on optical response

The absorption coefficient (α) was estimated using Eq. (10), while the extinction coefficient (k) was determined using Eq. (11). These parameters were subsequently used to calculate the refractive index (nnn) according to Eq. (12) and the real part of the dielectric constant (ε_r) using Eq. (13). The estimated bandgap values and the optical parameters selected for comparison are summarized in Table 5 [26][27].

$$\alpha = \frac{2.303A}{t} \quad (10)$$

$$k = \frac{\alpha\lambda}{4\pi} \quad (11)$$

$$n = \frac{1+\sqrt{R}}{1-\sqrt{R}} \quad (12)$$

$$\varepsilon_r = n^2 - k^2 \quad (13)$$

where A represent absorbance, R is reflectance, and t is film thickness.

Table 5. Estimated bandgap and selected optical parameters of $MAPbI_3$ thin films deposited under different spin-coating conditions.

Deposition speed (rpm)	E_g (eV)	Refractive index (n) at 886 nm	Dielectric constant (ε_r) at 886 nm
5000	1.59	2.32	4.86
4000	1.60	2.32	4.86
3000	1.60	2.16	4.36
2000	1.60	2.16	4.36

Figure 3(a) shows that all the $MAPbI_3$ films exhibit strong absorption throughout much of the visible region, followed by a pronounced decrease in absorbance toward the near-infrared region. The relative absorbance varies non-monotonically with spin-coating speed; notably, the $4000\ rpm$ film exhibits comparatively high absorbance in the shorter-wavelength region, while the relative ordering of the spectra changes with increasing wavelength. These differences may reflect the combined effects of spin-speed-dependent variations in film thickness, surface coverage, morphology, compactness, scattering, and microstructural characteristics, rather than changes in the intrinsic absorption strength of $MAPbI_3$ alone. However, because the film thicknesses were not independently measured, the specific contribution of thickness to the observed absorbance differences cannot be quantified.

The corresponding transmittance spectra show the complementary behaviour expected for the absorbing $MAPbI_3$ layers. Transmittance remains relatively low over the strongly absorbing visible region and increases markedly as the wavelength approaches the absorption edge. A pronounced change occurs at approximately $760 - 800\ nm$, beyond which the films become substantially more transparent. The relative transmittance of the samples also changes with wavelength rather than following a simple monotonic relationship with spin speed. This spectral crossing is consistent with differences in film thickness, optical interference, coverage and wavelength-dependent optical constants introduced by the different deposition conditions. Therefore, the transmittance response should be considered together with absorbance and film thickness rather than being used independently to rank film quality.

The calculated absorption coefficients remain of the order expected for strongly absorbing $MAPbI_3$ films throughout much of the visible spectrum and decrease rapidly near the fundamental absorption edge. The strong decline near approximately $775 - 780\ nm$ is consistent with the experimentally estimated bandgaps of $1.59 - 1.60\ eV$. For these bandgaps, the approximate band-edge wavelengths,

$$\lambda_g \approx \frac{1240}{E_g} \qquad 14$$

are about 780 nm for 1.59 eV and 775 nm for 1.60 eV, in agreement with the spectral edge observed in the optical measurements. The similarity of these absorption-edge positions indicates that changing spin speed substantially modifies the magnitude and spectral shape of the optical response without producing a large shift in the fundamental absorption threshold.

The wavelength-dependent refractive-index curves also show differences among the films. At 886 nm, the calculated refractive index is approximately 2.32 for the 4000 and 5000 rpm films and 2.16 for the 2000 and 3000 rpm films, with corresponding dielectric constants of 4.86 and

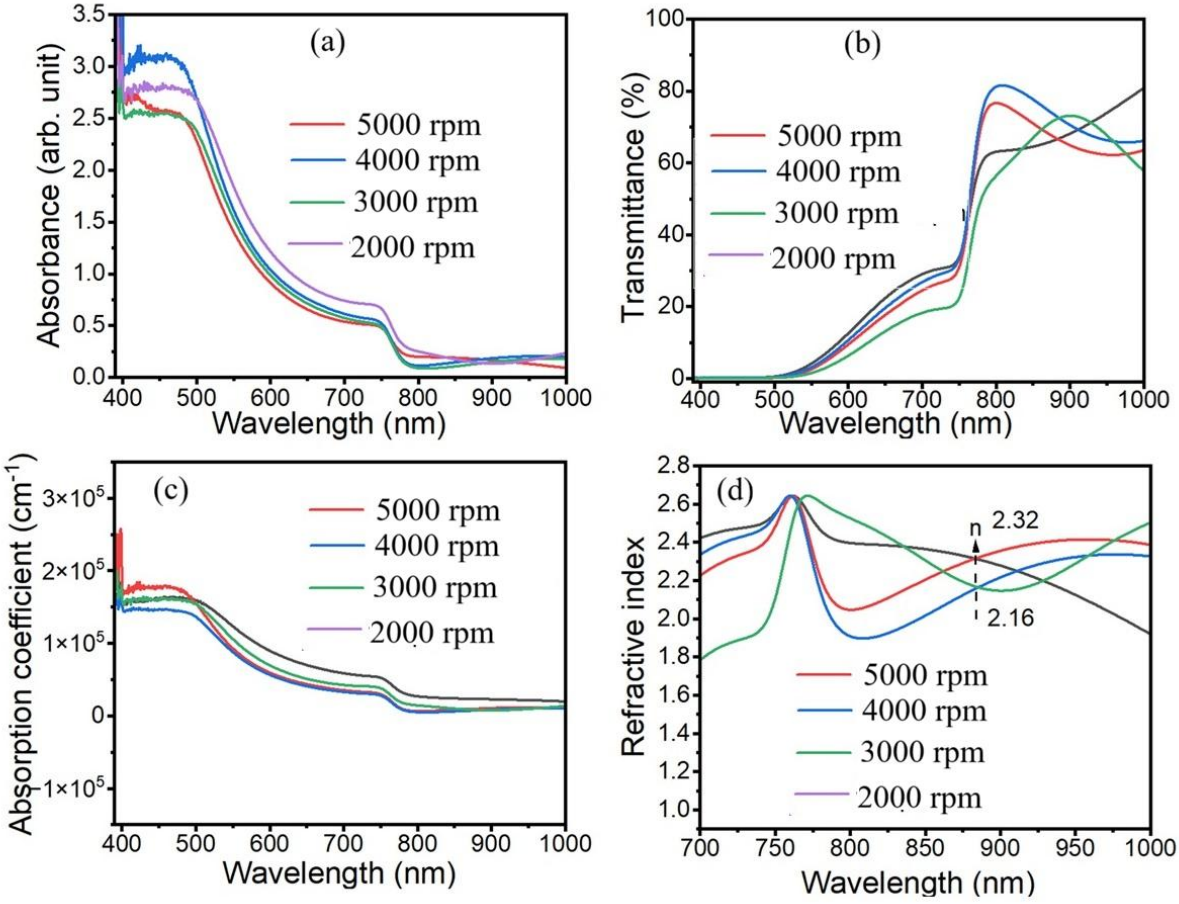


Fig. 3 (a) Optical absorption, (b) Optical transmittance, (c) Absorption coefficient, (d) Wavelength-dependent refractive index.

4.36, respectively. These differences suggest changes in the effective optical response of the films arising from the spin-coating conditions. However, because the refractive index was derived from the optical spectra rather than measured independently by ellipsometry, these values should be regarded as estimated effective optical parameters. Differences in thickness, surface roughness, scattering and reflectance may also contribute to the observed variation, and the refractive-index

values should therefore not be interpreted as direct evidence of fundamental changes in the intrinsic dielectric properties of $MAPbI_3$.

The optical-bandgap analysis yielded 1.59 eV for the film deposited at $5000\ rpm$ and 1.60 eV for the films deposited at 2000, 3000 and $4000\ rpm$. The slightly smaller bandgap of the $5000\ rpm$ film is consistent with the small red-shift of its estimated absorption edge. However, the difference is only:

$$\Delta E_g = 0.01\ eV$$

The $0.01\ eV$ difference represents only a marginal variation in the estimated optical bandgap and may lie within the uncertainty associated with Tauc extrapolation. Therefore, spin-coating speed produced no substantial change in the fundamental optical bandgap within the resolution of the present measurements.

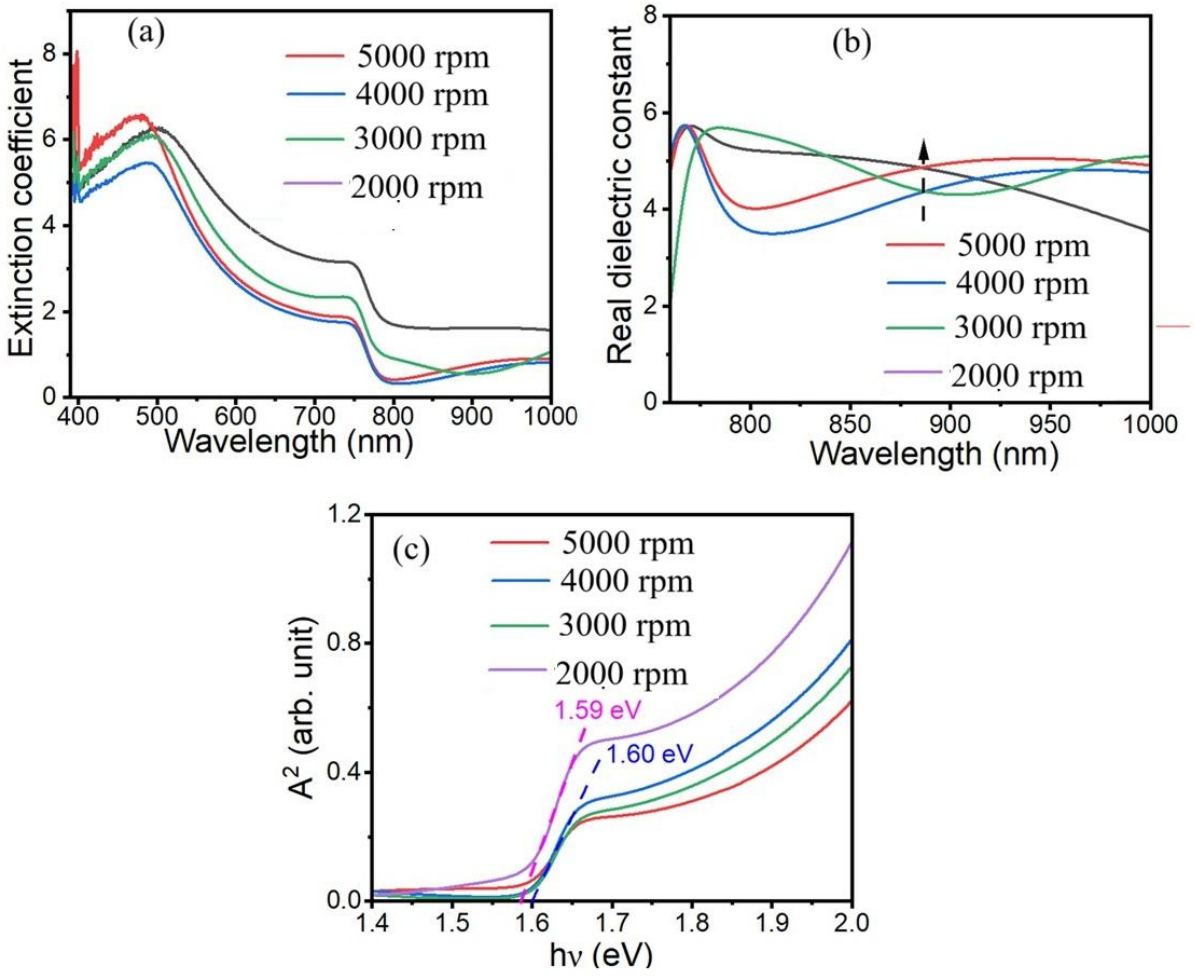


Fig. 4. (a) Extinction coefficient vs. wavelength, (b) Real dielectric constant vs. wavelength, (c) Graph of A^2 vs. hν for optical bandgap determination.

4. Assessment of photovoltaic performance by SCAPS-1D simulation

4.1 Bandgap-constrained comparison of baseline simulated devices

This section discusses the effect of bandgap of the prepared $MAPbI_3$ films on photovoltaic performance of simulated FTO/TiO_2/$MAPbI_3$/Spiro-OMeTAD/C PSC architecture. The literature reports that the bandgap of $MAPbI_3$ is one of the most important parameters controlling the photovoltaic performance of PSCs because it determines the spectral absorption range, open-circuit voltage (V_{OC}), short circuit current density (J_{SC}), and the power conversion efficiency (PCE) [28][29][30]. Shockley and Queisser [31] established that the photovoltaic efficiency limit of a single-junction solar cell is fundamentally determined by the absorber bandgap through the balancing between current generation and voltage loss. De Wolf et al. [32] further demonstrated that the sharp absorption edge and bandgap quality of perovskites are closely related to photovoltaic performance.

In this analysis, prototype devices were simulated to isolate the effect of the experimentally determined $MAPbI_3$ bandgap while keeping the absorber thickness and all other device parameters constant. The bulk-layer and interface-defect parameters used as inputs for the SCAPS-1D simulations are presented in Tables 2 and 3, respectively.

Only the experimentally determined bandgap of each deposited film was transferred into the prototype SCAPS-1D model. The XRD-derived coherent-domain size, microstrain and crystallographic dislocation-density parameter were not converted into SCAPS bulk- or interface-defect densities because no experimentally validated relationship was available for such a conversion. All other electronic parameters, including carrier mobility, doping concentration, bulk trap density, interface-defect density and recombination properties, were held constant. Therefore, the simulations isolate only the effect of the measured bandgap and cannot be used to rank the overall photovoltaic performance of films deposited at different spin-coating speeds.

Figure 5 presents the simulated performance of the FTO/TiO_2/$MAPbI_3$/Spiro-OMeTAD/carbon prototype cells using the experimentally determined $MAPbI_3$ bandgaps, while the corresponding photovoltaic parameters are summarized in Table 6. The prototype incorporating the 1.59 eV bandgap measured for the film deposited at 5000 rpm produced V_{OC}=1.10, J_{SC} =21.14 mA cm^{-2}, FF=71.85% and PCE=16.67%. The devices incorporating the 1.60 eV bandgaps measured for the films deposited at 2000, 3000 and 4000 rpm produced identical simulated values of V_{OC} =1.10 V, J_{SC} =20.92 mA cm^{-2}, FF=71.73% and PCE=16.47%, because they were assigned the same bandgap and otherwise identical model parameters. These results represent the isolated numerical effect of the 0.01 eV bandgap difference and not the complete influence of spin-coating speed or experimentally demonstrated device performance.

Table 6. Effect of bandgap of the prepared $MAPbI_3$ films on photovoltaic performance of the prototype PSCs

Deposition speed (rpm)	E_g (eV)	Photovoltaic performance			
		V_{OC} (V)	J_{SC} (mA/cm^2)	FF (%)	PCE (%)
5000	1.59	1.10	21.14	71.85	16.67
4000	1.60	1.10	20.92	71.73	16.47
3000	1.60	1.10	20.92	71.73	16.47
2000	1.60	1.10	20.92	71.73	16.47

Although the film deposited at 3000 rpm exhibited the most favourable XRD-derived crystalline characteristics, it did not produce the highest simulated prototype efficiency. The slightly higher simulated efficiency of 16.67% was obtained for the 5000 rpm film because its experimentally determined bandgap of 1.59 eV was marginally lower than the 1.60 eV values obtained for the other films. Because only the bandgap was varied while all other structural and electronic parameters were held constant, this result does not demonstrate that the 5000 rpm film would outperform the 3000 rpm film in an experimentally fabricated device. It instead confirms that the

present SCAPS-1D analysis cannot establish a direct relationship between the XRD-derived crystalline characteristics and photovoltaic performance.

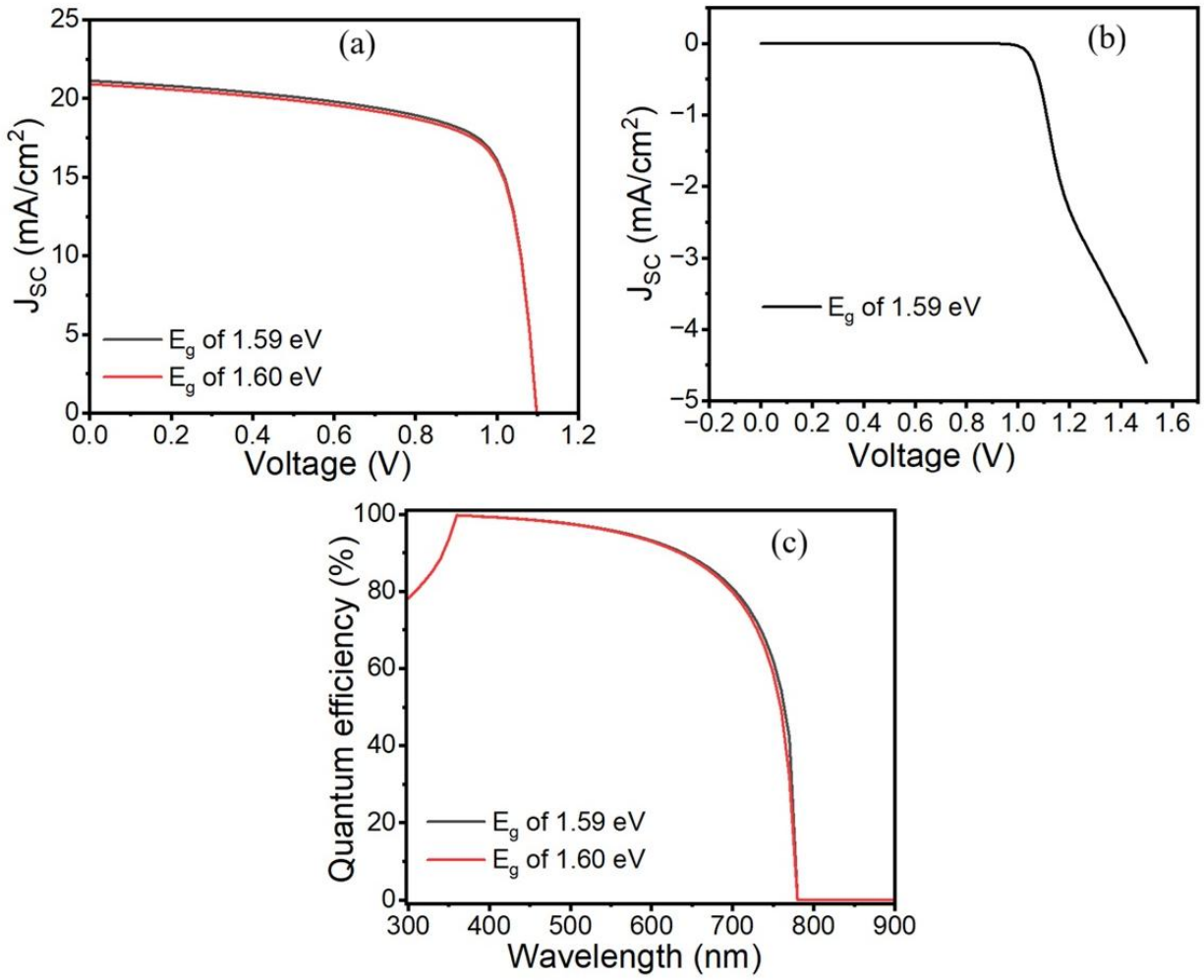


Fig. 5. (a) J-V plots under light for the PSCs obtained from the bandgaps of the synthesized $MAPbI_3$ absorber layer spin coated at varying speeds, (b) J-V plot under dark for the prototype device incorporating the experimentally measured bandgap of 1.59 eV. (c) Associated QE plots for device under illumination.

The PCE takes the combined effect of V_{OC} , J_{SC} , and FF according to Eq. 15**.**

$$PCE(\%) = \left(\frac{V_{OC} \times J_{SC} \times FF}{P_{in}}\right) \times 100 \qquad 15$$

The slightly higher J_{SC} of the 1.59 eV device results from its marginally broader absorption range. Its lower photon-energy threshold allows absorption of additional photons near the red edge of the solar spectrum, increasing electron–hole-pair generation and raising Jsc by approximately 1.05%. This behaviour is visible in Fig. 5a, where the illuminated J–V curves largely overlap, although the 1.59 eV cell shows a slightly higher current-density plateau. Because the transport, defect and resistance parameters were unchanged, the photocurrent increase is mainly optical rather than a consequence of improved transport or reduced recombination.

The simulated Voc remains unchanged because the 0.01 eV bandgap difference is too small to produce a visible variation at the reported precision. Moreover, Voc is also controlled by quasi-Fermi-level splitting, recombination, carrier concentrations, contacts and band alignment. The FF changes only slightly from 71.73% to 71.85%, indicating almost identical charge extraction, electric-field distribution and resistive losses in both devices.

The combined increase in Jsc and FF raises the PCE from 16.47% to 16.67%. Thus, the 1.59 eV absorber provides a slightly better balance between photon harvesting and voltage generation. Fig. 5c supports this interpretation, as the 1.59 eV cell has a slightly red-shifted absorption cut-off of about 780 nm compared with approximately 775 nm for the 1.60 eV cell, resulting in a marginally higher integrated photocurrent.

Figure 5b shows that the dark current of the 1.59 eV device remains low at small forward bias because the junction barrier and selective contacts restrict carrier injection. At higher forward voltage, the current rises rapidly as the barrier is reduced and diode injection and recombination become dominant. However, spin-coating speed can also modify film thickness, morphology, crystallinity, defect density and interface quality, which must be included separately to reproduce its full effect on device performance.

4.1.1 Energy-band characteristics

Fig. 6 presents the energy-band profiles of the FTO/TiO_2/$MAPbI_3$/Spiro-OMeTAD device for $MAPbI_3$ bandgaps of 1.60 and 1.59 eV under illumination, together with the dark-state profile of the 1.59 eV device. The plots show the conduction-band edge (E_C), valence-band edge (E_V), electron quasi-Fermi level (F_n), and hole quasi-Fermi level (F_p) across the device thickness. The conduction-band offset at the TiO_2/$MAPbI_3$ interface is −0.30 eV.

Thus, the interface exhibits a CBO of −0.30 eV, corresponding to a small cliff-like conduction-band alignment. This alignment promotes electron transfer from $MAPbI_3$ into TiO_2 because the TiO_2 conduction band lies approximately 0.30 eV below that of the absorber. However, an excessively large negative CBO could increase interfacial electron–hole recombination; therefore, control of the TiO_2/$MAPbI_3$ interface remains important.

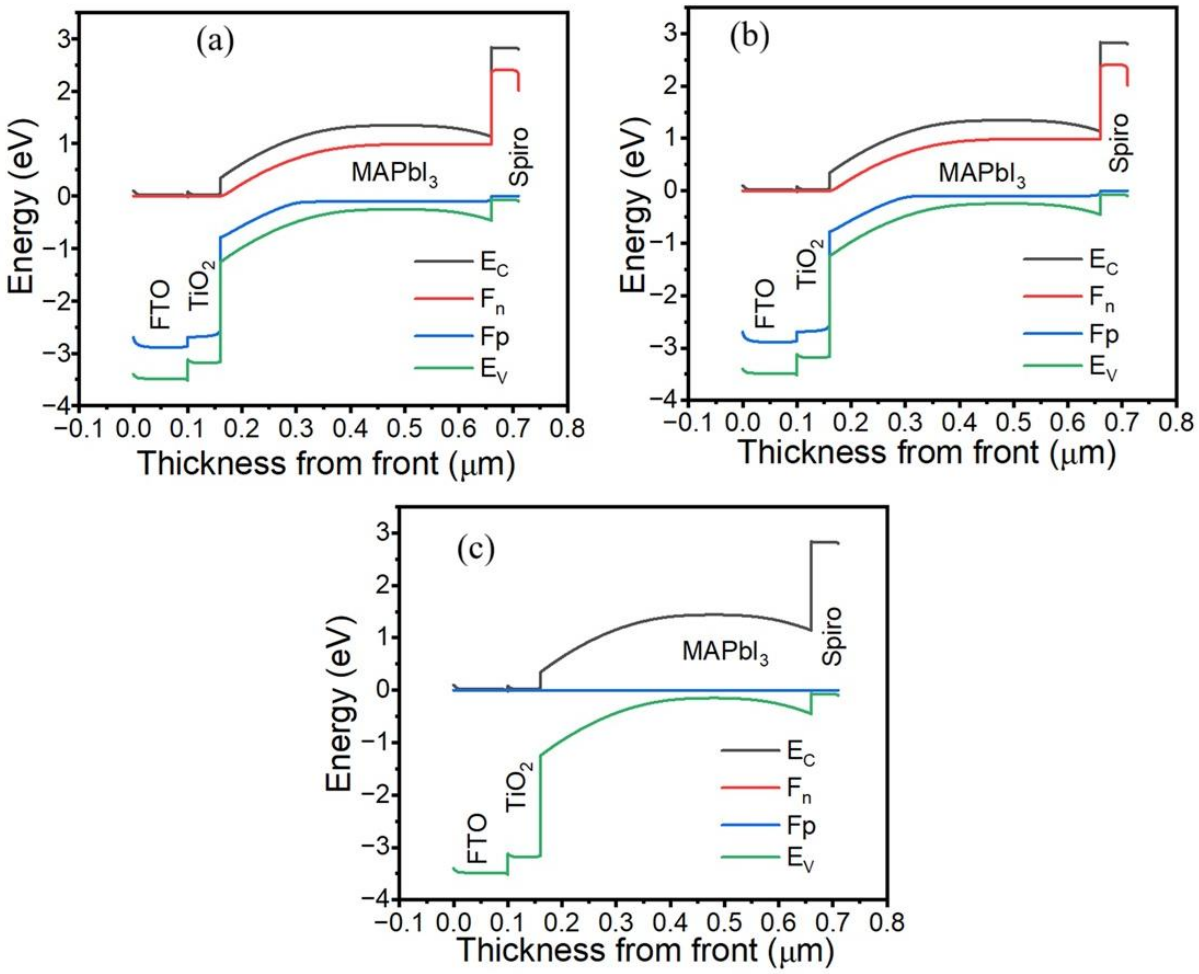


Fig. 6. (a) Energy band plots of the films with bandgap of 1.60 eV under illumination, (b) Energy band plots of the film with bandgap of 1.59 eV under illumination, (c) Energy band plots of the film with bandgap of 1.59 eV under dark.

The valence-band positions of $MAPbI_3$ are −5.49 and −5.50 eV for bandgaps of 1.59 and 1.60 eV, respectively. Consequently, the $MAPbI_3$/Spiro-OMeTAD interface has a valence-band offset

(VBO) magnitude of 0.41 eV for the 1.59 eV absorber and 0.40 eV for the 1.60 eV absorber. IN another convention, these correspond to −0.41 and −0.40 eV, respectively. The offset provides an energetic driving force for hole transfer into Spiro-OMeTAD, while its high conduction-band position blocks electrons from reaching the rear contact.

Under illumination, the bending of E_C and E_V across $MAPbI_3$ indicates an internal electric field that assists photogenerated-carrier separation. Electrons are directed towards TiO_2/FTO, while holes are transported towards Spiro-OMeTAD/carbon. The separation between F_n and F_p represents the light-induced quasi-Fermi-level splitting and is directly related to the generated photovoltage. The nearly identical splitting and band bending for the two absorber bandgaps agree with their common V_{OC} of 1.10 V.

Under dark conditions, F_n and F_p converge towards a common equilibrium Fermi level because excess photogenerated carriers are absent. Nevertheless, the band bending remains, demonstrating that the built-in field originates from equilibrium charge redistribution across the contacts and heterointerfaces.

4.2 Effect of layer thickness on photovoltaic performance

Fig. 7 shows that the photovoltaic response depends strongly on the function of each layer in the FTO/TiO_2/$MAPbI_3$/Spiro-OMeTAD/carbon device. Varying the TiO_2 thickness from 0.04 to 0.12 μm produces almost no change in V_{OC} or J_{SC}, while FF and PCE increase only slightly from 71.84 to 71.89% and from 16.66 to 16.68%, respectively (Fig. 7a). This weak dependence indicates that TiO_2 is already sufficiently thick for selective electron extraction and hole blocking throughout the investigated range. Because TiO_2 contributes little to useful photogeneration, further thickness increase provides no significant photocurrent benefit and only marginally modifies charge transport.

In contrast, $MAPbI_3$ thickness has the strongest influence on device performance. Increasing the absorber thickness from 0.5 to 1.0 μm raises Jsc from 21.14 to 22.86 mA/cm^2, FF from 71.85 to 77.51%, and PCE from 16.67 to 19.78%, while V_{OC} increases slightly from 1.10 to 1.12 V (Fig. 7b). A thicker absorber increases the optical path length and the probability that incident photons are absorbed, particularly near the band-edge region where the absorption coefficient is lower. The resulting increase in electron–hole-pair generation explains the improved Jsc and the enhanced

long-wavelength quantum efficiency in Fig. 8b. The modest increase in Voc is consistent with greater photogenerated carrier density and stronger quasi-Fermi-level splitting. The improved FF suggests that, within this simulated thickness range, the additional carrier generation outweighs transport and recombination losses. However, experimentally excessive absorber thickness may eventually increase bulk recombination because carriers must travel longer distances before collection.

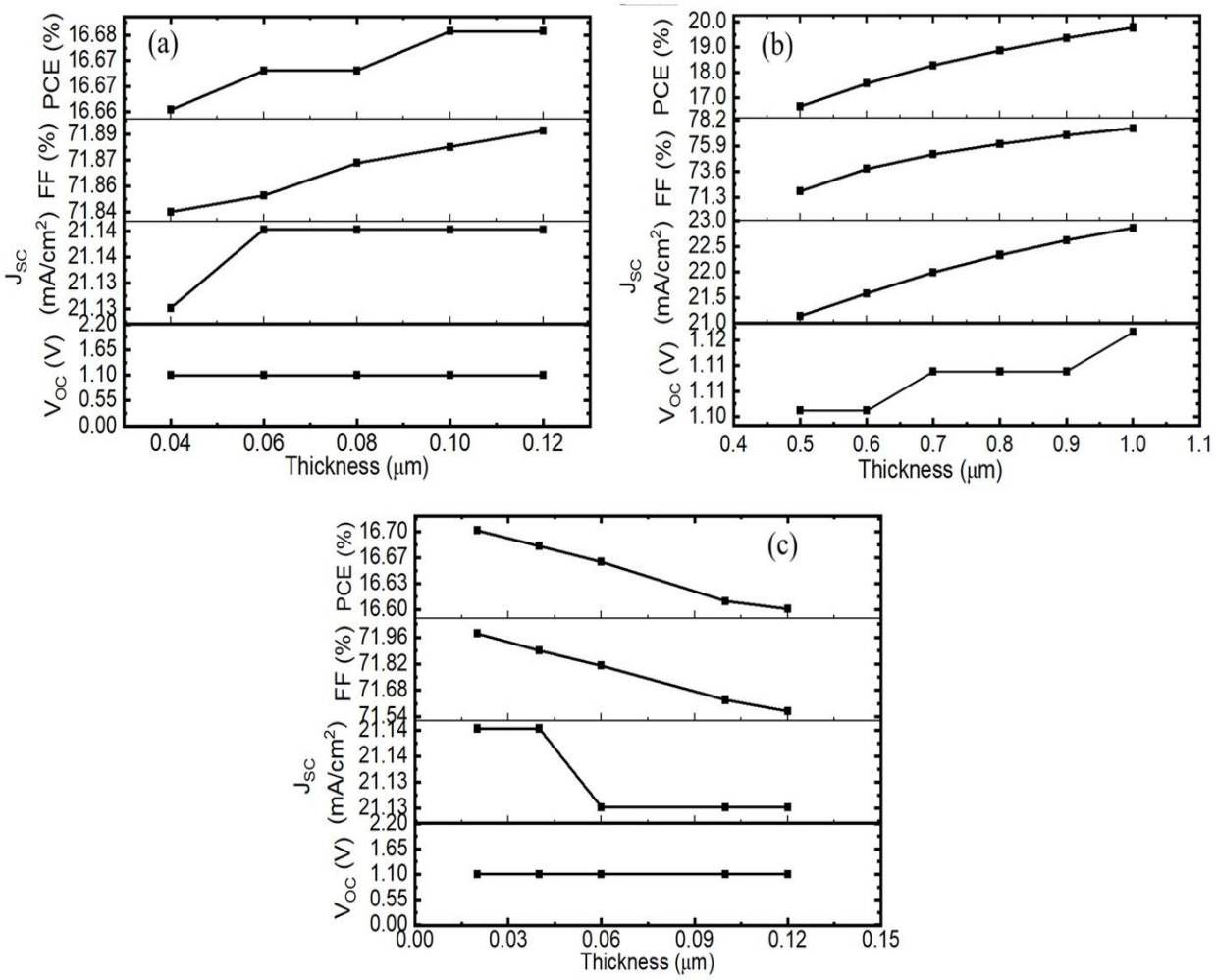


Fig. 7. (a) Dependence of V_{OC}, J_{SC}, FF and PCE on thickness of TiO_2, (b) Dependence of V_{OC}, J_{SC}, FF and PCE on thickness of $MAPbI_3$, (c) Dependence of V_{OC}, J_{SC}, FF and PCE on thickness of Spiro-OMeTAD.

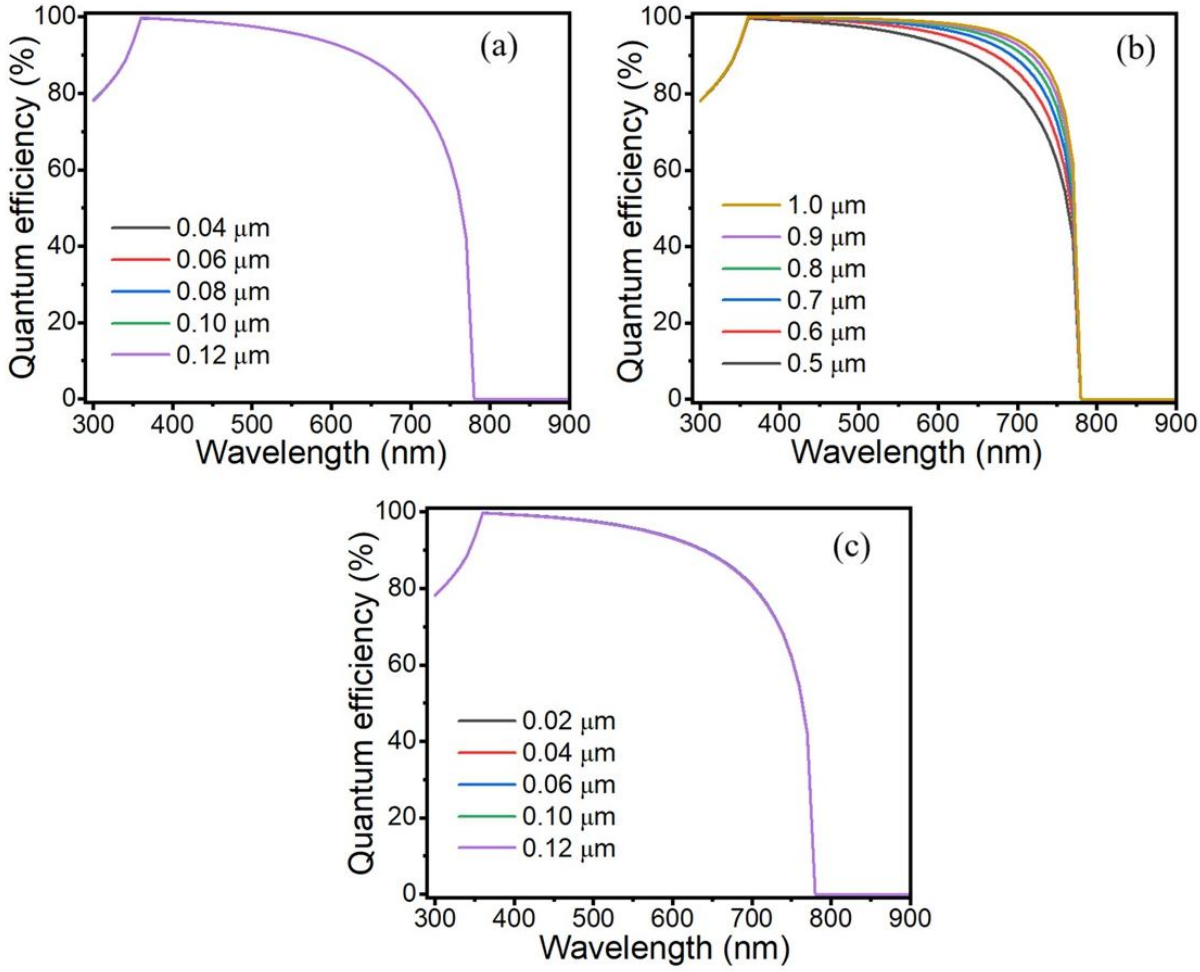


Fig. 8**.** QE plots for the effect of thickness of (a) TiO_2, (b) $MAPbI_3$, (c) Spiro-OMeTAD.

The Spiro-OMeTAD thickness produces the opposite trend. As its thickness increases from 0.02 to 0.12 µm, Voc and Jsc remain nearly constant, whereas FF decreases from 71.98 to 71.57% and PCE falls from 16.70 to 16.60% (Fig. 7c). Since Spiro-OMeTAD does not significantly contribute to photogeneration, increasing its thickness mainly lengthens the hole-transport pathway and raises the effective transport resistance. This increases the probability of carrier loss and slightly reduces charge-extraction efficiency. The nearly overlapping QE curves in Fig. 8c confirm that the effect is predominantly electrical rather than optical. Accordingly, the selected values of 0.12 µm TiO_2, 1.0 µm $MAPbI_3$ and 0.02 µm Spiro-OMeTAD provide the most favorable simulated performance within the investigated ranges.

4.3 Effect of Carrier density

Fig. 9 show that increasing the carrier density of both TiO_2 and Spiro-OMeTAD improves the photovoltaic performance of the FTO/TiO_2/$MAPbI_3$/Spiro-OMeTAD/carbon cell. The improvement is mainly associated with enhanced electrical conductivity, stronger selective-contact behaviour and more efficient extraction of photogenerated carriers. For TiO_2, increasing the donor density from 10^{14} to 10^{18} cm^{-3} raises Voc from 1.07 to 1.10 V, Jsc from 20.52 to 21.14 mA/cm^2, FF from 64.45 to 71.85%, and PCE from 14.18 to 16.67%. At low donor density, the relatively poor conductivity of TiO_2 increases electron-transport resistance and promotes carrier accumulation near the TiO_2/$MAPbI_3$ interface, which increases the probability of interfacial recombination. Higher donor density increases the electron concentration, lowers the resistive loss of the ETL and improves electron extraction towards FTO. It also shifts the TiO_2 Fermi level closer to the conduction band, strengthening the junction field and improving carrier separation. The pronounced rise in FF therefore reflects reduced transport resistance and recombination loss, while the modest increases in Voc and Jsc indicate improved quasi-Fermi-level splitting and charge collection.

A similar trend is observed for Spiro-OMeTAD. Increasing its acceptor density from 10^{15} to 10^{19} cm^{-3} increases Voc from 1.06 to 1.14 V, Jsc from 20.93 to 21.30 mA/cm^2, FF from 66.79 to 73.03%, and PCE from 14.82 to 17.71%. Higher acceptor density increases the hole concentration and conductivity of Spiro-OMeTAD, thereby reducing the resistance encountered by holes travelling towards the carbon electrode. It also reduces hole accumulation at the $MAPbI_3$/Spiro-OMeTAD interface and suppresses interfacial recombination. The resulting improvement in quasi-Fermi-level splitting produces the marked increase in Voc, while more efficient hole extraction improves FF and PCE.

The results further show that PCE is more sensitive to the carrier density of Spiro-OMeTAD than to that of TiO_2 over the investigated ranges. This indicates that hole extraction and transport through the HTL constitute a comparatively stronger limitation in the prototype cell.

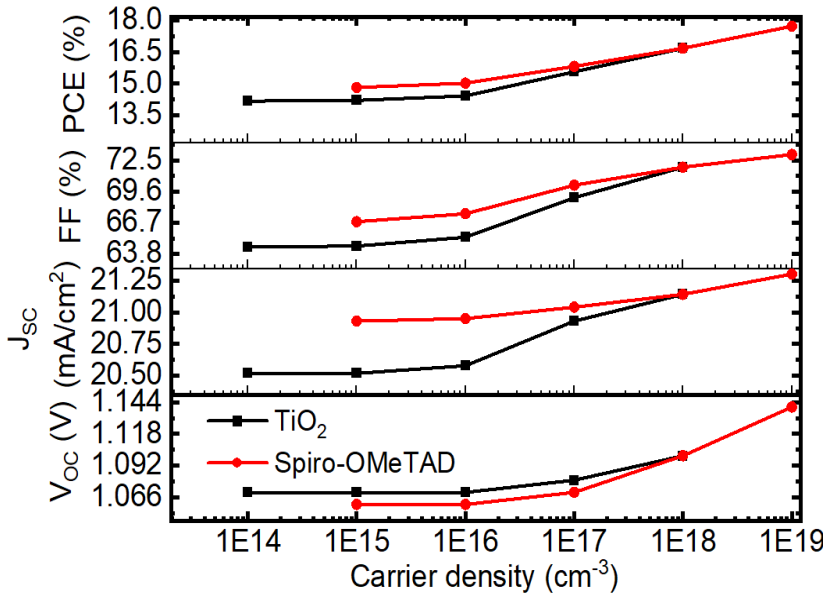


Fig. 9. Dependence of V_{OC}, J_{SC}, FF and PCE on carrier density of TiO_2 and Spiro-OMeTAD.

4.4 Effect of absorber bulk-defect density

Figure 10 illustrates the influence of $MAPbI_3$ bulk-defect density on the simulated photovoltaic parameters of the prototype device. Increasing the defect density from 10^{14} to 10^{19} cm^{-3} produced a strong and non-linear deterioration in all performance parameters. At the lowest investigated defect density of 10^{14} cm^{-3}, the device exhibited the most favourable simulated performance, with an open-circuit voltage Voc of 1.10 V, short-circuit current density J_{SC} of 21.14 mA cm^{-2}, fill factor (FF) of 71.85% and power-conversion efficiency (PCE) of 16.71%. When the defect density increased to 10^{16} cm^{-3}, Voc decreased slightly to 1.08 V, while J_{SC}, FF and PCE declined to 19.63 mA cm^{-2}, 65.01% and 13.78%, respectively.

A more pronounced deterioration occurred at higher defect densities. At 10^{18} cm^{-3}, Voc decreased to 0.95 V, J_{SC} fell sharply to 7.90 mA cm^{-2}, FF declined to 60.81% and PCE was reduced to 4.56%. A further increase in defect density to 10^{19} cm^{-3} reduced Voc to 0.82 V, J_{SC} to 2.46 mA cm^{-2}, FF to 55.50% and PCE to 1.12%. Across the investigated range of 10^{14} to 10^{19} cm^{-3}, Voc, J_{SC}, FF and PCE decreased by approximately 25.5%, 88.4%, 22.8% and 93.3%, respectively. The particularly severe reduction in J_{SC} indicates that photogenerated-carrier collection is highly sensitive to the assumed absorber bulk-defect density.

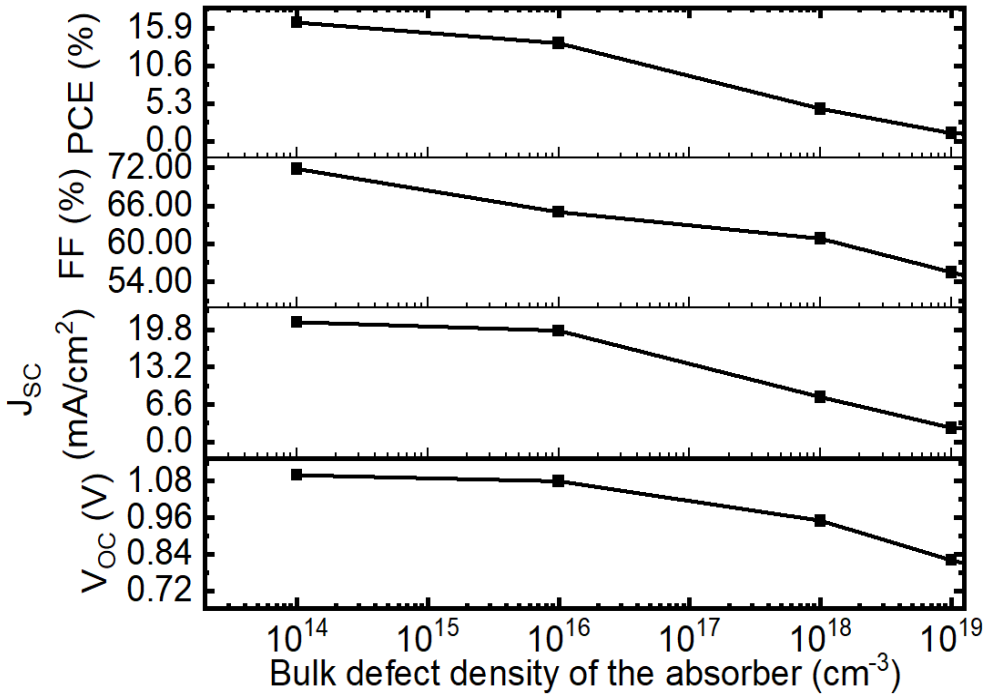


Figure 10. Simulated dependence of Voc, J_{SC}, FF and PCE on the $MAPbI_3$ absorber bulk-defect density.

The simulated deterioration can be attributed to the introduction of localized trap states within the $MAPbI_3$ bandgap. As the concentration of these states increases, electron and hole capture becomes more probable, enhancing trap-assisted Shockley–Read–Hall recombination. The resulting reduction in carrier lifetime and diffusion length increases the likelihood that photogenerated carriers will recombine within the absorber before reaching the TiO_2/$MAPbI_3$ and $MAPbI_3$/Spiro-OMeTAD interfaces. This mechanism accounts for the pronounced decline in J_{SC}. Increased trap-assisted recombination also limits electron–hole quasi-Fermi-level splitting, thereby lowering Voc. Furthermore, recombination losses and impaired carrier collection near the maximum-power point increase the non-ideal diode response and reduce FF. Because PCE depends on the combined values of Voc, J_{SC} and FF, the simultaneous degradation of these parameters produces the sharp efficiency decline observed in Figure 10.

These results indicate that the simulated device performs favourably only when the assumed $MAPbI_3$ bulk-defect density is maintained near the lower end of the investigated range. However, the defect densities examined in this analysis were SCAPS-1D input parameters and were not obtained from the XRD-derived coherent-domain size, microstrain or crystallographic dislocation-

density parameter of the deposited films. Figure 10 should therefore be interpreted as a numerical sensitivity analysis demonstrating the potential influence of electronically active bulk traps, rather than as direct evidence that a particular spin-coating condition produced the simulated defect density or photovoltaic performance.

4.5 Effect of interface-defect density

Fig. 11 and the corresponding tables show that increasing the interface-defect density degrades device performance by introducing interfacial trap states that capture photogenerated carriers and promote Shockley-Read-Hall recombination. The extent of the degradation, however, differs considerably between the TiO_2/$MAPbI_3$ and $MAPbI_3$/Spiro-OMeTAD interfaces.

At the TiO_2/$MAPbI_3$ interface, increasing the defect density from 10^{10} to 10^{14} cm^{-2} reduces V_{OC} from 1.11 to 1.01 V and PCE from 16.77 to 15.72%, while Jsc remains nearly constant at approximately 21.15 mA/cm^2. The nearly unchanged photocurrent indicates that electron collection through TiO_2 remains effective, even at relatively high interface-defect density. However, the additional traps increase electron–hole recombination near the ETL/absorber junction, reducing quasi-Fermi-level splitting and therefore Voc. The increase in FF from 71.43 to 73.64% does not indicate improved interface quality; rather, it partly compensates for the voltage loss and may arise from changes in the simulated J–V curvature. The overall reduction in PCE confirms that the net effect of increasing interface defects is detrimental.

The $MAPbI_3$/Spiro-OMeTAD interface is considerably more sensitive. Increasing its defect density from 10^{10} to 10^{14} cm^{-2} decreases Voc from 1.19 to 1.08 V, Jsc from 22.37 to 19.83 mA/cm^2, FF from 81.31 to 70.25%, and PCE from 21.71 to 15.03%. Trap states at this interface capture electrons and holes before selective hole extraction, enhancing non-radiative recombination and carrier accumulation. This reduces carrier lifetime, weakens quasi-Fermi-level splitting and increases extraction losses, accounting for the simultaneous decline in voltage, photocurrent and FF.

The stronger response of the rear interface indicates that hole extraction through the $MAPbI_3$/Spiro-OMeTAD junction is a major performance-limiting process in the prototype device. Consequently, reducing the defect density at this interface through improved film

coverage, chemical passivation and better interfacial contact should provide a larger efficiency gain than equivalent improvement at the TiO_2/$MAPbI_3$ interface.

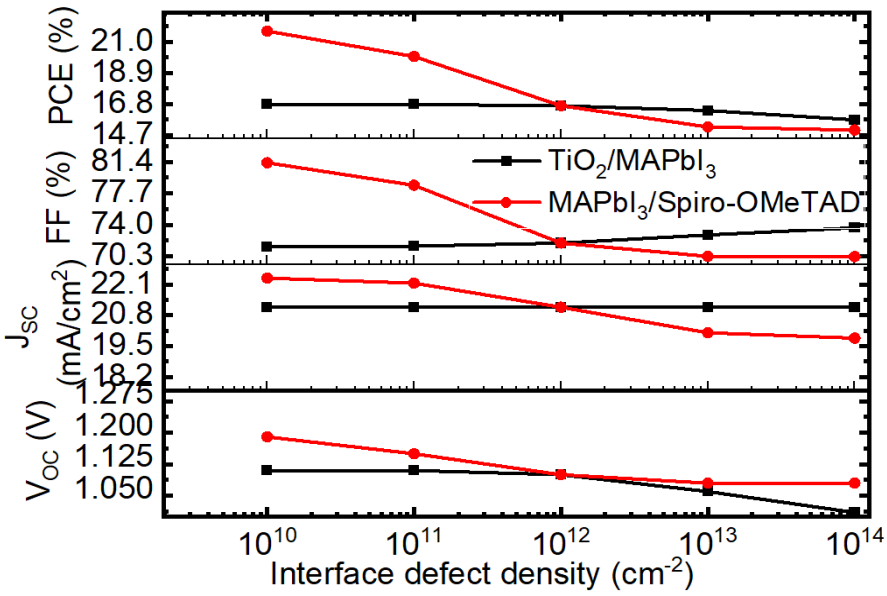


Fig. 11. Dependence of V_{OC}, J_{SC}, FF and PCE on defect density of TiO_2/$MAPbI_3$, and $MAPbI_3$/Spiro-OMeTAD interface.

4.6 Effect of series and shunt resistance

Fig. 12 shows that the photovoltaic response is highly sensitive to both series resistance and shunt resistance. Increasing from 0 to 50 Ωcm^2 reduces J_{SC} from 21.14 to 18.13 mA/cm^2, FF from 71.85 to 28.08%, and PCE from 16.67 to 5.59%, while V_{OC} remains nearly constant at 1.10 V.

Series resistance represents ohmic losses arising from the transport layers, electrodes, bulk materials and interfacial contacts. As series resistance increases, part of the photogenerated voltage is lost internally as an ($V = I.R_S$) drop, particularly near the maximum-power and short-circuit regions. This limits carrier extraction and distorts the illuminated J–V curve, producing the pronounced reduction in FF. The decrease in J_{SC} at high series resistance indicates that severe transport resistance also restricts the collection of photogenerated carriers. In contrast, V_{OC} is largely unaffected because the current is zero under open-circuit conditions and the associated resistive voltage drop is therefore negligible.

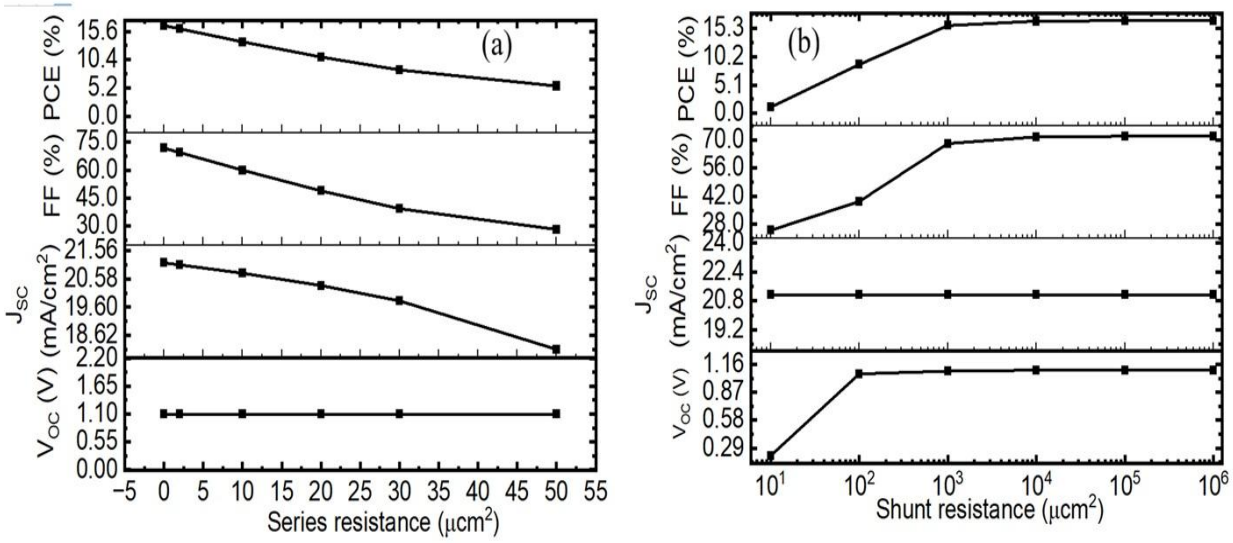


Fig. 12. Dependence of V_{OC}, J_{SC}, FF and PCE on (a) series and (b) shunt resistances of the stack device.

Shunt resistance exhibits the opposite effect. Increasing shunt resistance from 10^1 to 10^6 Ωcm^2 raises Voc from 0.21 to 1.10 V, FF from 24.98 to 71.85%, and PCE from 1.10 to 16.67%, whereas Jsc remains constant at 21.14 mA/cm^2. A low shunt resistance provides an alternative leakage pathway across the junction, allowing photogenerated current to bypass the external load. This leakage weakens the photovoltage, increases the slope of the J–V curve near short circuit and severely lowers FF and PCE. As shunt resistance increases, leakage becomes progressively suppressed, enabling more of the generated current to flow through the external circuit.

The improvement becomes small above approximately 10^4–10^5 Ωcm^2, indicating that shunt leakage is then negligible and other recombination or transport processes control performance.

4.7 Photovoltaic performance of the selected-parameter device

Simulations of the prototype device were used to identify suitable layer thicknesses of 0.12 μm for TiO_2, 1.0 μm for $MAPbI_3$, and 0.02 μm for the HTL. The HTL carrier density was slightly increased to 10^{19} cm^{-3}, while the bulk defect density of the ETL and HTL were reduced to 10^{14} cm^{-3}. The interface defect density was reduced to 10^{10} cm^{-2}. The selected defect-density ranges are

broadly consistent with values reported or adopted in previous experimental and numerical studies [33–38]. All other parameters remained unchanged as used in the prototype device.

Figure 13 demonstrates the improved photovoltaic response obtained after combining the favourable parameter values identified within the investigated ranges. At 300 K, the selected-parameter simulated device delivers V_{OC} of 1.25 V, J_{SC} of 24.24 mA/cm^2, FF of 83.61%, and PCE of 25.38%, representing a substantial improvement over the prototype efficiency of 16.67%. The projected PCE of 25.38% remains below the Shockley–Queisser efficiency limit for a single-junction absorber with a bandgap near 1.59 eV [39].

The more rectangular illuminated J-V curve in Fig. 13a indicates reduced transport and recombination losses. The higher J_{SC} originates mainly from the increased $MAPbI_3$ thickness, which improves photon absorption and photocarrier generation, while the higher Voc reflects reduced non-radiative recombination and stronger electron–hole quasi-Fermi-level splitting. The improved FF confirms more efficient carrier extraction, lower effective resistive losses and reduced carrier accumulation at the transport-layer interfaces.

The quantum-efficiency spectrum in Fig. 13b remains close to unity over most of the visible region before falling sharply near the $MAPbI_3$ absorption edge. This broad and high response demonstrates efficient photon-to-carrier conversion and collection across the absorber's active spectral range. The decline at longer wavelengths occurs because photons with energies below the $MAPbI_3$ bandgap cannot generate electron–hole pairs.

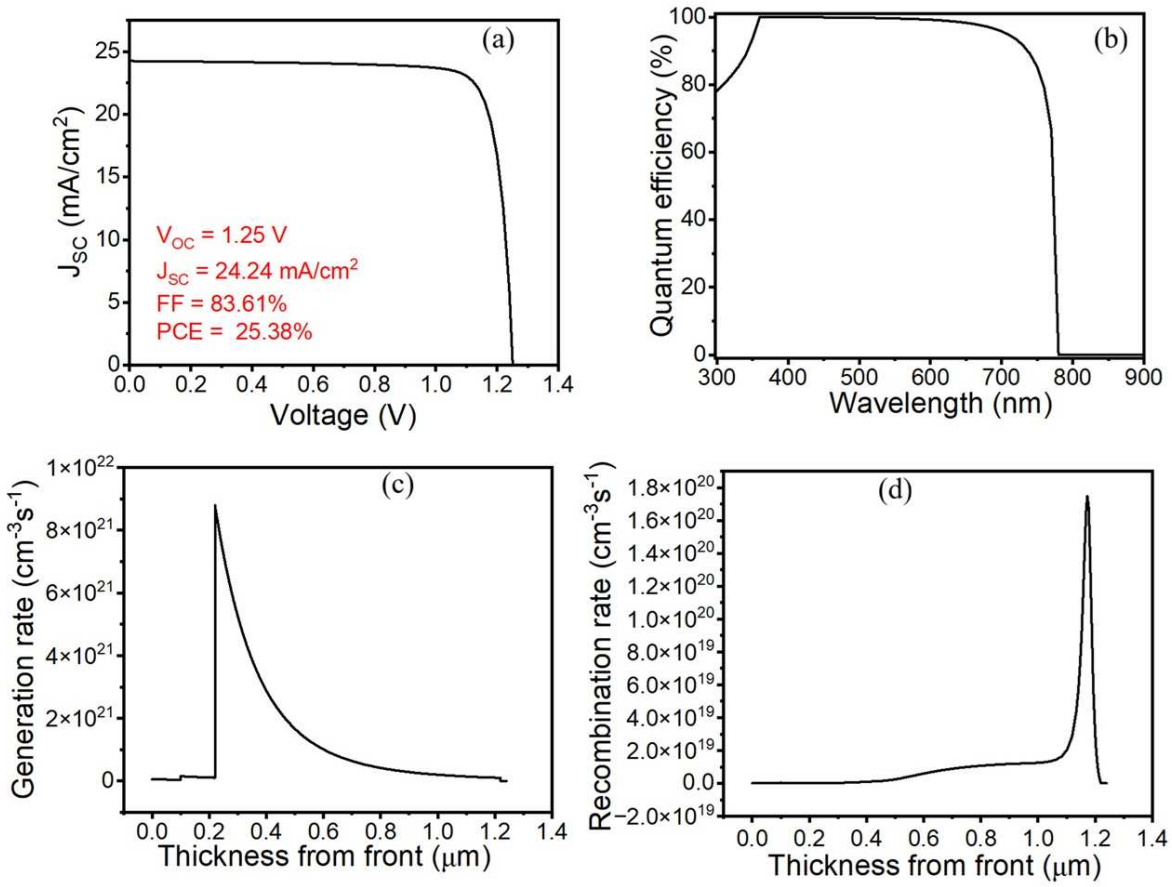


Fig. 13. (a) J-V curve for the optimized device, (b) QE plot, (c) Carrier generation rate, (d) Carrier recombination rate.

Figure 13c shows that carrier generation occurs predominantly within the $MAPbI_3$ absorber and is strongest near the illuminated TiO_2/$MAPbI_3$ side. This profile arises because the incident photon flux is greatest near the front of the device and decreases with penetration depth as light is progressively absorbed. The enlarged absorber thickness increases the integrated generation volume, thereby contributing to the enhanced photocurrent.

The recombination profile in Fig. 13d is substantially lower than the generation rate over most of the absorber, confirming that a large fraction of the generated carriers survives long enough to reach the selective contacts. The remaining recombination is concentrated near the heterointerfaces, where electrons and holes may coexist and interact with interfacial trap states. Reducing the bulk and interface defect densities to 10^{14} cm^{-3} and 10^{10} cm^{-2}, respectively, suppresses trap-assisted Shockley-Read-Hall recombination, increases carrier lifetime and

preserves the quasi-Fermi-level splitting. The predicted PCE of 25.38% is therefore governed not by a single parameter, but by the coordinated improvement of photogeneration, carrier lifetime, transport and collection throughout the device.

4.8 Effect of temperature on optimized device

Figure 14 shows the simulated response of the optimized device as the operating temperature was increased from 290 to 340 K while the user-defined material parameters were held constant. The simulated PCE decreased from 25.44% to 24.78%, principally because V_{oc} decreased from 1.26 to 1.21 V. In contrast, J_{sc} increased slightly from 24.24 to 24.28 $mA\ cm^{-2}$, while the fill factor increased from 83.24% to 84.50%.

Within the present fixed-parameter model, the reduction in V_{oc} is associated with the temperature-dependent carrier statistics, thermal velocities, thermal voltage, diffusion coefficients and their influence on carrier recombination and quasi-Fermi-level splitting. The nearly overlapping quantum-efficiency curves indicate that the simulated spectral response changes only slightly over the investigated temperature range.

Because the $MAPbI_3$ bandgap and optical-absorption parameters were held constant, the small increase in J_{sc} should not be attributed to bandgap narrowing or an extension of the absorption edge. Likewise, the simulation did not account explicitly for temperature-dependent mobility, dielectric properties, defect energetics, ionic migration or structural-phase changes.

The investigated range extends towards the tetragonal–cubic transition region of $MAPbI_3$ near 330 K. Because no phase-dependent material parameters were incorporated, the results should not be interpreted as a phase-resolved prediction of actual $MAPbI_3$ device behaviour across this transition. They instead describe the numerical temperature sensitivity of the assumed device parameter set.

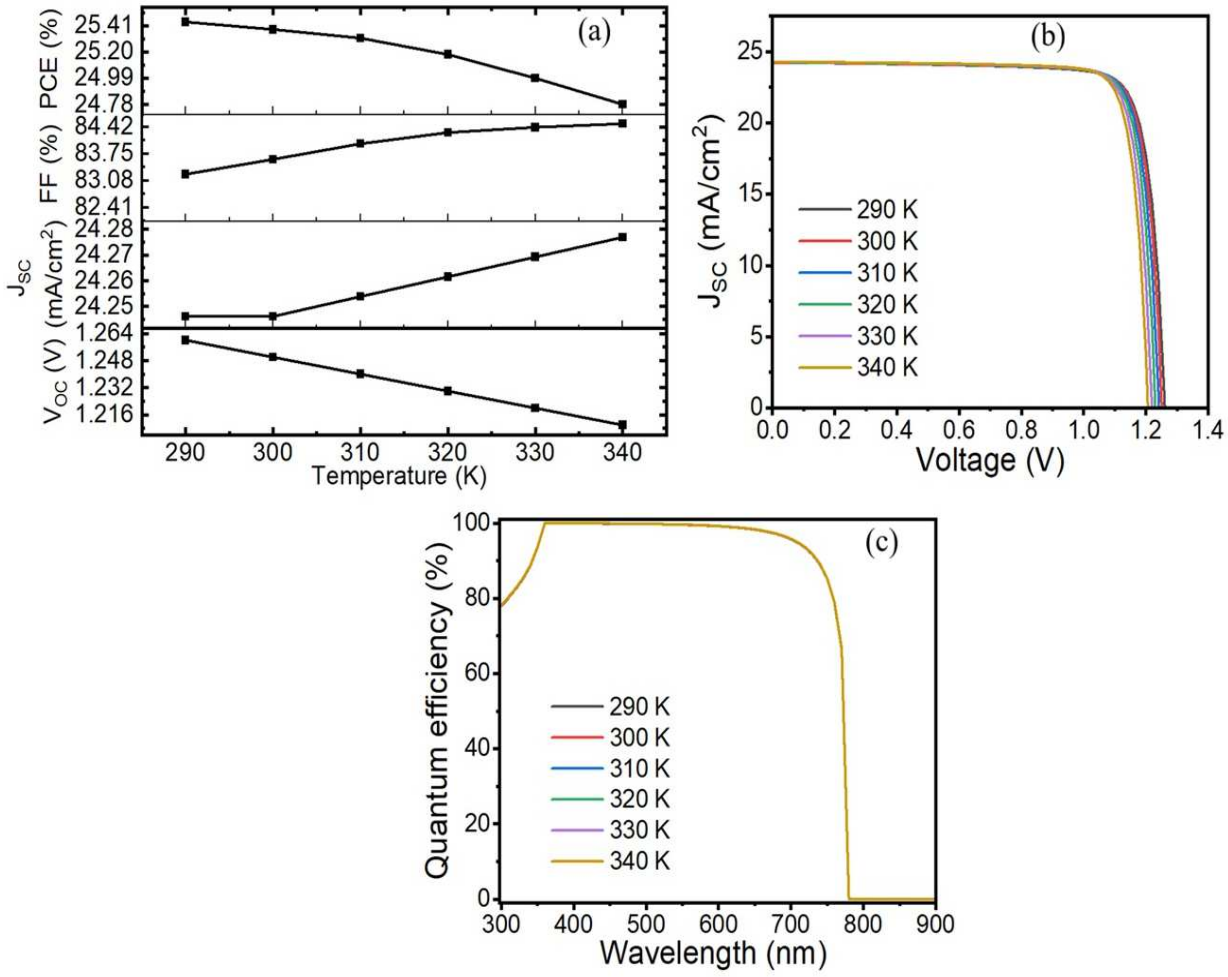


Fig. 14. (a) Dependence of V_{OC}, J_{SC}, FF and PCE on temperature of the device, (b) J-V curve for the effect of temperature, (c) QE plots.

4.9 Comparison with recent experimental and numerical studies

The present results are broadly consistent with recent studies showing that the optimum spin-coating condition for $MAPbI_3$ is not universal, but depends on the combined rates of wet-film thinning, solvent extraction, intermediate-phase conversion and thermal crystallization. Kılıç et al. [13] recently obtained their optimum ambient-air $MAPbI_3$ film at 4000 rpm for 40 s followed by annealing at 105 °C for 30 min. Their film showed dominant (110) orientation and no detectable PbI_2 phase. In the present study, the most favourable XRD-derived crystalline characteristics were obtained at 3000 rpm using a shorter 30 s coating cycle followed by annealing at 110 °C for 10 min. The agreement in phase identity and preferred orientation, but difference in optimum speed,

demonstrates that spin speed should be interpreted together with coating time, precursor/solvent system, antisolvent delivery and annealing schedule rather than as an independent universal control variable.

The Scherrer coherent-domain size of 22.73 nm estimated for the film deposited at 3000 rpm is lower than the approximately 33.38 nm reported for a fresh, ethyl-acetate-treated ambient $MAPbI_3$ film by Nur-E-Alam et al. [12]. Their toluene-treated film reached approximately 57.22 nm, further illustrating the strong dependence of coherent-domain size on antisolvent chemistry and processing history. Nevertheless, the XRD-derived parameters exhibit a non-monotonic trend under the investigated conditions, with the films deposited at 2000 and $5000\ rpm$ showing smaller coherent-domain sizes and higher microstrain than the film deposited at $3000\ rpm$. This indicates that either insufficient wet-film thinning at low speed or excessively rapid solvent removal at high speed can hinder ordered crystal growth. The absence of a detectable PbI_2 peak in the present films also agrees with the phase-pure ambient $MAPbI_3$ reported by Kılıç *et al*. [13].

The measured optical bandgaps of 1.59–1.60 eV fall within the commonly reported range for polycrystalline $MAPbI_3$, although they are slightly higher than the 1.57 eV obtained for an ethyl-acetate-processed film by Nur-E-Alam et al. [12] and the 1.53 eV reported by Rabhi et al. [17]. Differences of this magnitude can arise from precursor composition, thickness, strain, phase purity, optical baseline treatment and the method used to construct the Tauc plot. The narrow 0.01 eV spread across the present samples indicates that varying spin speed changed crystallite-related structural quality much more strongly than the intrinsic absorption threshold. Consequently, the small simulated performance difference between the 1.59 and 1.60 eV prototype absorbers should not be interpreted as the complete photovoltaic effect of spin speed, because experimentally induced changes in thickness, coverage, grain boundaries and defect density were held constant in that particular simulation.

The optimized SCAPS-1D efficiency of 25.38% is also credible relative to recent numerical $MAPbI_3$ studies, but it remains model-dependent. Ali et al. [18] reported 23.32% after optimizing $MAPbI_3$ and transport-layer thicknesses, incorporating Ti_3C_2 MXene and examining temperature effects. Rabhi et al. [17] predicted 28.39% for an experimentally informed but different AZO/SnO_2/$MAPbI_3$/D-PBTTT-14/RGO architecture. The present value lies between these reports. Its difference from 23.32% or 28.39% should not be treated as a direct ranking because the studies

used different electrodes, transport materials, band offsets, optical losses, mobilities and defect assumptions. More importantly, the reduction of $MAPbI_3$ bulk-defect density and interface-defect density in the present optimization explains much of the increase from the 16.67% prototype to 25.38%, confirming that recombination control is at least as important as the small measured bandgap variation.

The present results establish 3000 rpm as the condition yielding the most favourable XRD-derived crystalline characteristics for the investigated formulation and processing protocol. This designation is limited to phase formation, diffraction-peak broadening and the associated microstructural estimates. It does not demonstrate that the 3000 rpm film possesses the lowest electronic trap density, longest carrier lifetime or highest photovoltaic efficiency. Moreover, because only the experimentally determined bandgap was transferred into SCAPS-1D, the simulations do not establish a causal relationship between the XRD parameters and predicted device performance.

Table 7. Comparison of the present results with recent experimental and SCAPS-1D studies of $MAPbI_3$.

Study	**Processing/model distinction**	**Main reported outcome**	**Relation to this work**
This study	Ambient $MAPbI_3$; EA antisolvent; 2000–5000 rpm; 110 °C, 10 min	Most favourable XRD-derived crystalline characteristics at 3000 rpm; D = 22.73 nm; Eg = 1.59–1.60 eV; optimized SCAPS PCE = 25.38%	Reference case
Nur-E-Alam *et al.* (2024) [12]	Ambient $MAPbI_3$; four antisolvents; ≈300 nm films	EA: D = 33.38 nm and Eg = 1.57 eV; EA gave the lowest degradation among the tested antisolvents	Supports EA use; shows antisolvent-dependent crystallite size and bandgap

Study	Processing/model distinction	Main reported outcome	Relation to this work
Rabhi *et al.* (2024) [17]	Experimental $MAPbI_3$ plus SCAPS; alternative AZO/SnO_2/$MAPbI_3$/D-PBTTT-14/RGO stack	Tetragonal $MAPbI_3$; Eg = 1.53 eV; optimized PCE = 28.39%	Higher predicted PCE reflects different transport layers, contacts and assumptions
Ali *et al.* (2025) [18]	SCAPS $MAPbI_3$ optimization with Ti_3C_2 MXene and layer-thickness/temperature studies	Optimized PCE = 23.32%	Present 25.38% lies within the range of recent optimized simulations
Kılıç *et al.* (2026) [13]	Ambient one-step $MAPbI_3$; 4000 rpm, 40 s; 105 °C, 30 min	Dominant (110) orientation; no detectable PbI_2	Confirms ambient feasibility; different optimum demonstrates process dependence

5. Limitations of the structural–device correlation

The principal limitation of the present study is that XRD-derived crystallite size, microstrain and the estimated crystallographic dislocation-density parameter describe coherent lattice order but do not directly quantify electronically active point defects, deep-level traps or non-radiative recombination. Photoluminescence, time-resolved photoluminescence, space-charge-limited-current, impedance-spectroscopy and complete-device measurements were not performed. Therefore, no direct causal relationship can be established between the XRD parameters and photovoltaic performance. Furthermore, the SCAPS-1D defect densities were literature-based or parametrically varied inputs rather than experimentally measured properties of the individual films. The simulations should consequently be interpreted as bandgap-constrained sensitivity analyses and device-design projections, not as predictions of the relative device performance of the four spin-coated films.

6. Conclusion

This study established a process-specific relationship between spin-coating speed and the structural and optical properties of open-air-processed $MAPbI_3$ thin films. XRD confirmed preferentially (110)-oriented tetragonal $MAPbI_3$ without a detectable PbI_2 reflection under the investigated conditions. Among the tested speeds, 3000 rpm produced the narrowest (110) diffraction peak, largest Scherrer coherent-domain size and lowest estimated microstrain and crystallographic dislocation-density parameter. It is therefore identified as the condition yielding the most favourable XRD-derived crystalline characteristics for the present precursor formulation, ethyl-acetate treatment and annealing protocol. This finding should not be interpreted as direct evidence of the lowest electronic trap density or the best photovoltaic performance.

The films exhibited optical bandgaps of 1.59–1.60 eV. When these measured values were introduced into an otherwise fixed SCAPS-1D model, the 1.59 eV absorber produced a simulated efficiency of 16.67%, compared with 16.47% for the 1.60 eV absorbers. Because the model varied only the experimental bandgap while holding thickness and electronic defect parameters constant, this small difference represents the isolated effect of bandgap and not the complete influence of spin-coating speed. The optimized efficiency of 25.38% is consequently a model-dependent projection based on coordinated changes in several assumed device parameters rather than an experimentally demonstrated efficiency.

Direct verification of the relationship between deposition speed and photovoltaic performance requires measurements of carrier lifetime and recombination, electronic trap density, mobility and complete-device characteristics. Future work should therefore combine steady-state and time-resolved photoluminescence, space-charge-limited-current or impedance measurements with replicated J-V, external quantum-efficiency and stabilized-output measurements for devices fabricated from each deposition condition.

Competing Interests

The authors have no relevant financial or non-financial interests to disclose

Acknowledgement

This work was supported by the UKRI Ayrton Fund: REACH-PSM – Resilient Renewable Energy Access through Community-Driven Holistic Development in Perovskite Solar Module Manufacturing.

Data Availability

The data for this work will be made available on request.

Ethics, Consent to Participate, and Consent to Publish declarations

Not applicable.

Funding

This study was undertaken within the broader UKRI Ayrton Fund–supported REACH-PSM project. However, the fund did not provide specific financial support for the preparation or writing of this manuscript.

Authors Contributions

Aaron O. Aransiola – Conceptualization, Investigation, Methodology, Writing – Original Draft

Peverga R. Jubu - Conceptualization, Methodology, Writing, Data Curation, Software, Writing – Original Draft

Chijioke Amakom – Conceptualization, Methodology, Writing, Data Curation, Review and Editing

Kufre I. Udofia – Conceptualization, Methodology, Writing, Data Curation, Review and Editing

Izuchukwu K. Nwokolo - Conceptualization, Methodology, Data Curation, Writing – review and editing

Adamu Ahmed Goje - Conceptualization, Methodology, Data Curation, Writing – review and editing

John O. Anyanwu –Data Curation, Writing – review and editing

Ikechukwu I. Ayogu - Review and Editing

Kanayo Lucy Oguzie - Review and Editing

Muhammad B. Kuranga – Software

Olusoji O. Ilori – Supervision, Validation

S. P. Olayiwola – Review and Editing

O. O. Fadahunsi - Review and Editing

Chinyere A. Madu – Supervision, Validation

Emeka E. Oguzie - Supervision, Funding acquisition, Validation

References

1. Kojima, A.; Teshima, K.; Shirai, Y.; Miyasaka, T. Organometal halide perovskites as visible-light sensitizers for photovoltaic cells. Journal of the American Chemical Society 2009, 131 (17), 6050–6051. https://doi.org/10.1021/ja809598r.
2. Lee, M. M.; Teuscher, J.; Miyasaka, T.; Murakami, T. N.; Snaith, H. J. Efficient hybrid solar cells based on meso-superstructured organometal halide perovskites. Science 2012, 338 (6107), 643–647. https://doi.org/10.1126/science.1228604.
3. Jena, A. K.; Kulkarni, A.; Miyasaka, T. Halide perovskite photovoltaics: background, status, and future prospects. Chemical Reviews 2019, 119 (5), 3036–3103. https://doi.org/10.1021/acs.chemrev.8b00539.
4. Stranks, S. D.; Eperon, G. E.; Grancini, G.; Menelaou, C.; Alcocer, M. J. P.; Leijtens, T.; Herz, L. M.; Petrozza, A.; Snaith, H. J. Electron–hole diffusion lengths exceeding 1 micrometer in an organometal trihalide perovskite absorber. Science 2013, 342 (6156), 341–344. https://doi.org/10.1126/science.1243982.
5. De Wolf, S.; Holovsky, J.; Moon, S.-J.; Löper, P.; Niesen, B.; Ledinsky, M.; Haug, F.-J.; Yum, J.-H.; Ballif, C. Organometallic halide perovskites: sharp optical absorption edge and its relation to photovoltaic performance. The Journal of Physical Chemistry Letters 2014, 5 (6), 1035–1039. https://doi.org/10.1021/jz500279b.
6. Herz, L. M. Charge-carrier dynamics in organic–inorganic metal halide perovskites. Annual Review of Physical Chemistry 2016, 67, 65–89. https://doi.org/10.1146/annurev-physchem-040215-112222.
7. Correa-Baena, J.-P.; Saliba, M.; Buonassisi, T.; Grätzel, M.; Abate, A.; Tress, W.; Hagfeldt, A. Promises and challenges of perovskite solar cells. Science 2017, 358, 739–744. https://doi.org/10.1126/science.aam6323.
8. Green, M. A.; Ho-Baillie, A.; Snaith, H. J. The emergence of perovskite solar cells. Nature Photonics 2014, 8, 506–514. https://doi.org/10.1038/nphoton.2014.134.

9. Emslie, A. G.; Bonner, F. T.; Peck, L. G. Flow of a viscous liquid on a rotating disk. Journal of Applied Physics 1958, 29, 858–862. https://doi.org/10.1063/1.1723300.
10. Jeon, N. J.; Noh, J. H.; Kim, Y. C.; Yang, W. S.; Ryu, S.; Seok, S. I. Solvent engineering for high-performance inorganic–organic hybrid perovskite solar cells. Nature Materials 2014, 13, 897–903. https://doi.org/10.1038/nmat4014.
11. Xiao, M.; Huang, F.; Huang, W.; Dkhissi, Y.; Zhu, Y.; Etheridge, J.; Gray-Weale, A.; Bach, U.; Cheng, Y.-B.; Spiccia, L. A fast deposition-crystallization procedure for highly efficient lead iodide perovskite thin-film solar cells. Angewandte Chemie International Edition 2014, 53 (37), 9898–9903. https://doi.org/10.1002/anie.201405334.
12. Nur-E-Alam, M.; Islam, M. A.; Kar, Y. B.; Kiong, T. S.; Misran, H.; Khandaker, M. U.; Fouad, Y.; Soudagar, M. E. M.; Cuce, E. Anti-solvent materials enhanced structural and optical properties on ambiently fabricated perovskite thin films. Scientific Reports 2024, 14 (1), 19995. https://doi.org/10.1038/s41598-024-70344-3.
13. Kılıç, M.; Özdal, T.; Kavak, H. Optimization of $MAPbI_3$ photoactive layer via cost-effective single-step spin-coating under ambient air condition. Optical and Quantum Electronics 2026, 58 (4), 180. https://doi.org/10.1007/s11082-026-08752-0.
14. Wall, E. M.; Lin, Y.-K.; Bawendi, M.; Burlingame, Q. C.; Loo, Y.-L. Impact of processing environment on anti-solvent-free $FAPbI_3$ films and solar cells. Advanced Energy Materials 2026, 16(7), e03828. https://doi.org/10.1002/aenm.202503828.
15. Burgelman, M.; Nollet, P.; Degrave, S. Modelling polycrystalline semiconductor solar cells. Thin Solid Films 2000, 361–362, 527–532. https://doi.org/10.1016/S0040-6090(99)00825-1.
16. Decock, K.; Khelifi, S.; Burgelman, M. Modelling multivalent defects in thin film solar cells. Thin Solid Films 2011, 519(21), 7481-7484. https://doi.org/10.1016/j.tsf.2010.12.039
17. Rabhi, S.; Sekar, K.; Kalna, K.; et al. Experimental findings and SCAPS-1D simulations for high-efficiency $MAPbI_3$ perovskite solar cells beyond 31%. Optical and Quantum Electronics 2024, 56(8), 1372. https://doi.org/10.1007/s11082-024-07282-x.
18. Ali, S.; Khan, M. Q.; Khan, R. A.; et al. Improved photovoltaic performance of $MAPbI_3$-based solar cells via SCAPS. Indian Journal of Physics 2025, 99, 4667–4675. https://doi.org/10.1007/s12648-025-03649-2.
19. M. K. Hossain, S. Islam, M. N. Sakib, M. S. Uddin, G. F. I. Toki, M. H. K. Rubel, J. Nasrin, S. H. Shahatha, M. R. Mohammad, A. A. Alothman, C. J. Raorane, R. Haldhar, and H. Bencherif,

"Exploring the optoelectronic and photovoltaic characteristics of lead-free Cs_2TiBr_6 double perovskite solar cells: A DFT and SCAPS-1D investigation", Advanced Electronic Materials 11 (2025) 1. https://doi.org/10.1002/aelm.202400348.

20. P.R. Jubu, Z.S. Mbalaha, E.V. Tikyaa c, O.S. Obaseki, K.O. Ighodalo, O. Adedokun, A. Nathan-Abutu, M.B. Ochang, Y. Yusof, M.Z. Pakhuruddin. High-efficiency hole transport layer-free perovskite solar cells utilizing TiO2, ZnO and bilayer TiO2/ZnO electron transport layers: A simulation approach. Next Materials 9 (2025) 1-17. https://doi.org/10.1016/j.nxmate.2025.101166
21. E. Danladi, E. E. Oguzie, and F. I. Ezema, "Highly efficient 25.562% $Cs_2AgBiBr_6$ double perovskite solar cell with copper barium tin sulfide and ZnO as charge transport channels: an intuition from a theoretical study using SCAPS-1D", Journal of Photonics for Energy 15 (2025) 024501. https://doi.org/10.1117/1.JPE.15.024501
22. J. He; Yu Bai; Zhixin Luo; Ran Ran; Wei Zhou; Wei Wang; Zongping Shao. Advanced carbon-based rear electrodes for low-cost and efficient perovskite solar cells. Energy Environ. Sci. (2025) 18 (5): 2136–2164. https://doi.org/10.1039/d4ee05462h
23. M. Baro and P. Borgohain, "SCAPS-1D device simulation of highly efficient perovskite solar cells using diverse charge transport layers," *Journal of Electronic Materials*, vol. 52, pp. 7623–7644, 2023. DOI: 10.1007/s11664-023-10681-7
24. Y. Raoui, H. Ez-Zahraouy, N. Tahiri, O. El Bounagui, S. Ahmad and S. Kazim, "Performance analysis of $MAPbI_3$-based perovskite solar cells employing diverse charge-selective contacts: Simulation study," *Solar Energy*, vol. 193, pp. 948–955, 2019. DOI: 10.1016/j.solener.2019.10.009
25. P.R. Jubu, F.K. Yam, K.T. Low. Feasibility study on synthesis of gallium oxide nanostructures on glass substrate by chemical vapor deposition. Thin Solid Films 710 (2020) 1-7. https://doi.org/10.1016/j.tsf.2020.138257
26. P. R. Jubu, E. Danladi, M.B. Ochang, O. Adedokun, C.C. Amadi, D.D. Hile, W.V. Zhiya, A.A. Iorokpen, Y. Yusof, F.K. Yam. Influence of the content of stacked ZnO on the structural and optical properties of heterostructured ZnO/Ga_2O_3 films. Optical Materials: X 21 (2024) 100291. https://doi.org/10.1016/j.omx.2024.100291
27. P.R. Jubu, T.T. Bem, U.I. Ndeze, E. Danladi, P.I. Kyesmen, V. Mbah, S. Benourdja, D.D. Hile, A.B. Atsuwe, F.K. Yam. Optical and optoelectronic properties of gallium oxide films

fabricated by the chemical vapour deposition method. *Physica B: Condensed Matter 678 (2024) 415763.* Doi: https://doi.org/10.1016/j.physb.2024.415763

28. Fakharuddin, A., Vasilopoulou, M., Soultati, A., Haider, M.I., Briscoe, J., Fooulos, V., Di Girolamo, D., Davazoglou, D., Chroneos, A., Yusoff, A.R.b.M., Abate, A., Schmidt-Mende, L. and Nazeeruddin, M.K. (2021), Robust Inorganic Hole Transport Materials for Organic and Perovskite Solar Cells: Insights into Materials Electronic Properties and Device Performance. Sol. RRL, 5: 2000555. https://doi.org/10.1002/solr.202000555
29. Miah MH, Khandaker MU, Rahman MB, Nur-E-Alam M, Islam MA. (2024). Band gap tuning of perovskite solar cells for enhancing the efficiency and stability: issues and prospects. RSC Adv.14(23):15876-15906. https://doi.org/ 10.1039/d4ra01640h.

Sha, W.E.I., Ren, X., Chen, L., Choy, W.C.H. (2015). The Efficiency Limit of $CH_3NH_3PbI_3$ Perovskite Solar Cells. Appl. Phys. Lett. 106, 221104. https://doi.org/10.1063/1.4922150

31. Shockley, W., & Queisser, H. J. (1961). Detailed balance limit of efficiency of p-n junction solar cells. Journal of Applied Physics, 32, 510–519. doi: 10.1063/1.1736034.

32. De Wolf, S., Holovsky, J., Moon, S.-J., Löper, P., Niesen, B., Ledinsky, M., Haug, F.-J., Yum, J.-H., & Ballif, C. (2014). Organometallic halide perovskites: sharp optical absorption edge and its relation to photovoltaic performance. Journal of Physical Chemistry Letters, 5(6), 1035–1039. DOI:10.1021/jz500279b
33. Chowdhury, M. S.; Shahahmadi, S. A.; Chelvanathan, P.; Tiong, S. K.; Amin, N.; Techato, K.; Nuthammachot, N.; Chowdhury, T.; Suklueng, M. Effect of deep-level defect density of the absorber layer and n/i interface in perovskite solar cells by SCAPS-1D. Results in Physics 16 (2020) 102839. https://doi.org/10.1016/j.rinp.2019.102839
34. Khac, D.L., Chowdhury, S., Luengchavanon, M., Jamal, M.S., Laref, A. et al. Influence of deep-level defect of absorber layer and n/i interface on the performance of antimony triselenide solar cells by numerical simulation. Sustainability 14(11), 6780 (2022). Doi: 10.3390/su14116780
35. Srivastava, S., Singh, S. & Singh, V.K. Bulk and interface defects analysis of n-CdS/p-Si heterojunction solar cell. Opt. Mater. 111, 110687 (2021). Doi: 10.1016/j.optmat.2020.110687

36. Li, Y., Ding, B., Chu, Q.Q., et al.: Ultra-high open-circuit voltage of perovskite solar cells induced by nucleation thermodynamics on rough substrates. Scientific Reports 7, 46141 (2017). https://doi.org/10.1038/srep46141.
37. Moot, T., Patel, J.B., McAndrews, G., et al.: Temperature coefficients of perovskite photovoltaics for energy yield calculations. ACS Energy Letters 6 (2021) 2038–2047. https://doi.org/10.1021/acsenergylett.1c00748.
38. Singh, P., Ravindra, N.M.: Temperature dependence of solar cell performance—an analysis. Solar Energy Materials and Solar Cells 101 (2012) 36–45. https://doi.org/10.1016/j.solmat.2012.02.019.
39. S. Rühle, "Tabulated values of the Shockley–Queisser limit for single junction solar cells", Solar Energy 130 (2016) 139-147. https://doi.org/10.1016/j.solener.2016.02.015